AFFDL-TR-64-189

ACTIVE CONTROL OF BOOSTER ELASTICITY

ROBERT L. SWAIM

TECHNICAL REPORT AFFDL-TR-64-189

APRIL 1965

AIR FORCE FLIGHT DYNAMICS LABORATORY
RESEARCH AND TECHNOLOGY DIVISION
AIR FORCE SYSTEMS COMMAND
WRIGHT-PATTERSON AIR FORCE BASE, OHIO

AFFDL-TR-64-189

ACTIVE CONTROL OF BOOSTER ELASTICITY

ROBERT L. SWAIM

FOREWORD

This report presents the results of in-house research conducted by Robert L. Swaim, Flight Control Division, Air Force Flight Dynamics Laboratory, Research and Technology Division, Air Force Systems Command, Wright-Patterson Air Force Base, Ohio. The work was initiated under Project No. 8219, "Stability and Control Investigations," Task No. 821901, "Aerothermoelastic Effects on Stability and Control." This is a final report and concludes the work on the program started in October 1963 and completed in August 1964. The manuscript was released by the author in December 1964 for publication as an RTD Technical Report.

This technical report has been reviewed and is approved.

W. A. SLOAN, JR.
Colonel, USAF
Chief, Flight Control Division
Air Force Flight Dynamics Laboratory

ABSTRACT

An investigation was made of the problem of providing an automatic control system for a large booster subject to severe mode interaction. This interaction is defined as a strong aerodynamic coupling between the rigid-body motion and one or more elastic modes of the vehicle and can appear as a flutter phenomenon between rigid and elastic degrees of freedom as opposed to "classical" flutter between two or more elastic degrees of freedom. For the booster considered, the interaction resulted in a rigid-body mode static divergence for an aerodynamically, statically stable, rigid configuration in the uncontrolled or forward-loop-only system. It was shown that preliminary control system design must include the significant elastic modes when mode interaction is present. A rigid-body-only synthesis will not yield "ball-park" values for the control element gains.

The investigation revealed that the active control philosophy of using auxiliary control inputs to increase the frequencies of the elastic modes sufficient to reduce the mode of interaction in the forward-loop is a false notion. It is the free-free bending modes which interact with the rigid-body motion, and input forces cannot alter their mode shapes and frequencies. They can be altered only by mass and structural stiffness changes to the basic vehicle. The input forces result in changes to elastic mode coupled frequencies and damping ratios which do not affect the mode interaction phenomenon as defined in this report.

Analysis has shown that it is meaningless to specify desired transient response in terms of closed-loop, short-period frequency and damping ratio as a criterion for control system synthesis when the vehicle is subject to severe mode interaction. In general, the closed-loop modes cannot be identified as being elastic or rigid-body in the conventional sense. In this case new synthesis criteria are needed. Perhaps a better approach would be to specify desired time histories for the various controlled variables.

BLANK PAGE

TABLE OF CONTENTS

ILLUSTRATIONS

ILLUSTRATIONS (Continued)

TABLES

LIST OF SYMBOLS

a_o	acceleration tangent to steady state flight path (ft/sec^2)
$C_N(\ell)$	local normal force coefficient based on total vehicle planform area (1/ft)
$C_{N_\alpha}(\ell)$	local slope of normal force coefficient curve ($\frac{1}{\text{ft-rad}}$)
F_A	aerodynamic force in z-direction (lbs)
F_T	component of thrust in z-direction (lbs)
F_z	sum of F_A and F_T (lbs)
F_r	force from reaction jet (lbs)
g	acceleration of gravity (ft/sec^2)
G	denotes point of thrust application
h	altitude (ft)
I_y	total mass moment of inertia about CG in xz-plane (slugs-ft^2)
K_A	amplifier gain
K_c	actuator gain (1/sec)
K_r	inner-loop actuator gain (1/sec)
K_R	rate gyro gain (sec)
K_z	displacement sensor gain (sec)
ℓ	coordinate of length, positive aft from nose (ft)
ℓ_r	absolute distance from nose to reaction jet location (ft)
ℓ_G	absolute distance from CG to point of thrust application (ft)
ℓ_{CG}	absolute distance from nose to CG (ft)
ℓ_z	absolute distance from nose to displacement sensor (ft)
L	total configuration length (ft)
m	mass per unit length (slugs/ft)
m_p	mass flow rate (slugs/sec)

LIST OF SYMBOLS (Continued)

M	total configuration mass (slugs)
M_o	total configuration mass at launch (slugs)
M_A	aerodynamic moment about CG, positive nose up (ft-lbs)
M_T	moment about CG due to component of thrust in z-direction, positive nose up (ft-lbs)
M_y	sum of M_A and M_T (ft-lbs)
$q_D = \frac{1}{2} \rho U^2$	dynamic pressure (lbs/ft^2)
$q_1(t), q_2(t)$	first and second elastic modes' generalized coordinates normal to centerline, positive in negative z-direction (ft)
Q_{1A}, Q_{2A}	generalized aerodynamic forces in z-direction (lbs)
Q_{1T}, Q_{2T}	generalized thrust components in z-direction (lbs)
Q_{1z}, Q_{2z}	sums of Q_{1A}, Q_{1T}, and Q_{2A}, Q_{2T} (lbs)
s	Laplace variable (1/sec)
S	total configuration planform area (ft^2)
S_r	general reference area for aerodynamic coefficients (ft^2)
t, τ	time (sec)
T	thrust magnitude (lbs)
$\frac{1}{T_{1sp}}, \frac{1}{T_{2sp}}$	coupled short-period mode real roots (1/sec)
u	perturbation velocity in x-direction (ft/sec)
U	undisturbed (steady state) velocity in x-direction (ft/sec)
$\overline{z}$	signal from high-pass filter (ft)
x, z	stability axes coordinates in disturbed state (ft)
Z_{CG}	displacement of CG normal to steady-state, rigid centerline (ft)
α	perturbation angle of attack (rad)
α_g	angle of attack due to gusts and wind shear (rad)

LIST OF SYMBOLS (Continued)

γ	perturbation flight path angle (rad)
γ_o	undisturbed flight path angle (rad)
δ	thrust vector deflection with respect to missile elastic axis, positive up (rad)
δ_r	actuating signal to reaction jet valving mechanism (ft)
δ_1 , δ_2	error signals
ζ_1 , ζ_2	structural damping ratios of first and second elastic modes
ζ_{sp}	short-period mode damping ratio
ζ_{sp_c}	coupled short-period mode damping ratio
ζ_{1e} , ζ_{2e}	damping ratios of first and second coupled elastic modes
θ	perturbation rigid-body pitch angle, positive nose up (rad)
θ_o	undisturbed rigid-body pitch angle, positive nose up (rad)
θ_i	total perturbation pitch angle at gyro location (rad)
$\bar{\theta}_i$	signal from low-pass filter (rad)
θ_c	input command pitch signal (rad)
θ_E	pitch angle error signal (rad)
θ_F	pitch angle feedback signal (rad)
$\xi(\ell,t)$	elastic deflection normal to rigid centerline, positive in negative z-direction (ft)
$\xi(G,t)$	elastic deflection at point of thrust application (ft)
$\frac{\partial \xi(G,t)}{\partial \ell}$	slope of elastic axis at point of thrust application (rad)
ρ	free stream air density (slugs/ft^3)
$\sigma_1(\ell)$, $\sigma_2(\ell)$	negative slopes of normalized mode shapes (1/ft)
$\sigma_1(G)$, $\sigma_2(G)$	negative slopes of normalized mode shapes at point of thrust application (1/ft)

LIST OF SYMBOLS (Continued)

$\sigma_1(RG), \sigma_2(RG)$	negative slopes of normalized mode shapes at gyro location (1/ft)
$\phi_1(r), \phi_2(r)$	values of normalized mode shapes at reaction jet location
$\phi_1(\ell), \phi_2(\ell)$	local values of normalized mode shapes
$\phi_1(G), \phi_2(G)$	values of normalized mode shapes at point of thrust application
$\phi_1(z), \phi_2(z)$	values of normalized mode shapes at displacement sensor location
ω_1, ω_2	undamped natural frequencies of elastic modes (rad/sec)
ω_{sp}	short-period undamped natural frequency (rad/sec)
ω_{sp_c}	coupled short-period undamped natural frequency (rad/sec)
ω_{1e}, ω_{2e}	undamped natural frequencies of coupled elastic modes (rad/sec)
$\mathcal{M}_1 = \int_0^L m\phi_1^2 \, d\ell$	generalized mass of first elastic mode (slugs)
$\mathcal{M}_2 = \int_0^L m\phi_2^2 \, d\ell$	generalized mass of second elastic mode (slugs)
$A_\theta, A_{q_1}, A_{q_2}$	numerical gains
$N_\theta, N_{q_1}, N_{q_2}$	normalized numerator polynomials
Δ	normalized characteristic polynomial
$N_{\theta\delta_r}$	numerator of (θ/δ_r) transfer function

INTRODUCTION

The design of an automatic control system for a large booster is a very complicated and difficult problem since dynamic aeroelastic degrees of freedom must be included in the analysis. In addition to stabilizing and controlling the rigid-body motion along a prescribed boost trajectory, the control system must be designed to preclude any instabilities in the elastic modes due to structural feedback. This normally has been accomplished by the use of various filtering and shaping networks in the control system mechanization. The normal or usual approach has been first to establish tentative values for the major control element gains which will give the desired closed-loop rigid-body dynamics. This constitutes an analysis of a set of very simplified equations of motion in which the transfer functions of the various system elements have been taken in their simplest approximate form. Once the tentative gains have been selected, more sophisticated analyses are carried out in which the elastic modes are included along with other significant dynamic effects such as propellant sloshing and control engine oscillations. Conventional synthesis techniques are then used in various stages of complexity to arrive at the electronic networks required to ensure compatible and stable performance of the total system. To date most aeroelastic effects have been successfully handled by this rather passive approach of designing around the elasticity to avoid aeroelastic problems with no attempt to actively control it, which would involve a change in the total energy state of the elastic modes.

It will be shown in this report that active control of some of the lower frequency vibration modes will likely be mandatory from a flight control point of view on some future highly flexible boosters, not to mention that structural stiffness requirements may also dictate such control. By providing suitably phased control inputs the stiffness and damping of the structural dynamics can be artificially augmented, allowing the booster to tolerate larger aerodynamic loads without an increase in structural weight or, conversely, tolerate the same loading with a lighter structure.

From the flight control aspect, some form of active elastic mode control may be necessitated by the adverse effects produced by "mode interaction." This interaction is defined as a strong aerodynamic coupling between the rigid-body motion and one or more elastic modes of the vehicle and is, in fact, a flutter phenomenon between rigid and elastic degrees of freedom as opposed to "classical" flutter between two or more elastic degrees of freedom. Mode interaction can occur when the frequencies of one or more elastic modes and the transient rigid-body motion are of the same order of magnitude. The physical reason for this will become apparent when the governing equations of motion are developed and analyzed later. Such an interaction can drive one or more of the modes involved unstable.

As booster designs become larger, the percentage of structural weight to total weight usually decreases. This means the structural vibration mode frequencies will be lower. And since the desired rigid-body transient dynamics are relatively independent of size for large boosters, the frequency spread between rigid-body transient motion and the elastic vibration modes becomes less. These conditions for severe mode interaction will likely be present on some future boosters, making control system design extremely complex and difficult since they prevent the designer from carrying out his preliminary design based only on rigid-body dynamics.

There is a school of thought that says by actively controlling the lower frequency vibration modes, that is, artificially adding stiffness and damping by properly phased and sized control inputs, coupled natural frequencies can be increased to the point where these modes no longer have an appreciable interaction with the rigid-body transient dynamics. The validity of this premise is the primary subject of this report.

In Section I the equations of motion describing the transient dynamics of a typical booster along a prescribed trajectory are derived. In Section II the kinematic trajectory equations are developed and time histories of the trajectory parameters plotted. The chosen vehicle mass data and elastic characteristics are also given. Section III contains an analysis of the forward-loop dynamics; that is, no control loops are included. Section IV considers the closed-loop dynamics resulting from the addition of a feedback loop to augment the short-period pitch response dynamics. Section V introduces active control of the two lowest frequency elastic modes using a single inner-loop sensor and actuation by the main engine thrust vector. The closed-loop dynamics are analyzed for this type control. Section VI studies the case where two inner-loop sensors are used in the active control. Section VII considers the use of a separate actuating system for the elastic modes consisting of a single reaction jet, leaving the main engine thrust vector for rigid-body control. Section VIII contains conclusions and recommendations and Section IX lists references cited in the text.

SECTION I

PERTURBATION EQUATIONS OF MOTION

The essence of the coupling between rigid-body and elastic vibration modes for large boosters can be demonstrated by considering only the rigid-pitch and plunge degrees of freedom (short-period approximation) and the elastic modes of interest. The analysis will be confined to motion in the longitudinal (vertical) plane only, since it is in this plane that the predominant forces are developed. The rigid degree of freedom in the direction of the vehicle longitudinal axis can be uncoupled from the others by assuming perturbation drag is not a function of angle of attack. Thus, the forward velocity is unperturbed by attitude changes. This assumption removes any consideration of a "phugoid" mode. It is justified on the basis that change in aerodynamic drag due to perturbations in angle of attack is a small force relative to the propulsive and inertial forces; hence, this change has a negligible effect on velocity history. Also, the system analyzed is one of accelerated motion, having no steady flight condition in which a low frequency phugoid mode can manifest itself. The predominant coupling with the two-degree-of-freedom rigid-body motion is provided by the low frequency elastic modes in the longitudinal plane. For purposes of this analysis only the two lowest frequency elastic modes will be included, thereby assuming the remaining modes to be of sufficiently high frequency to avoid coupling with the rigid-body motion. The contribution of these higher-order modes to the sensor signals being fed back to the automatic control system can be eliminated by the standard techniques of low-pass filtering and, if necessary, gain stabilization. Therefore a four-degree-of-freedom system must be analyzed. Later on, additional degrees of freedom will be introduced by the control system equations of motion.

The type of configuration considered is a large, multistage booster with a rigid, lifting-payload and rigid stabilizing fins (Figure 1). The assumption of solid propellant, fixed rocket engines is made to simplify the analytical description of the forcing functions acting on the vehicle. This eliminates consideration of fuel sloshing forces which a liquid propellant system would introduce. Also, by assuming thrust vectoring by a means such as secondary gas injection, the inertial forces which would be present with gimballing control engines are avoided. The booster body structure is assumed to be highly flexible and susceptible to relative motion between structural elements. Such motion will occur in parallel mountings of solid propellant cores.

In deriving the equations of motion based on linearized small perturbations about a given trajectory, a right-hand stability (Eulerian) axes system is used, with the x axis aligned initially with the relative velocity lying in the x-z plane (see Figure 2). The rigid-body and first two elastic mode perturbation equations are (in terms of the generalized masses, coordinates, and forces of the two elastic modes)

$$MU(\dot{\alpha} - \dot{\theta}) = F_z - Mg\theta \sin\gamma_0 \tag{1}$$

$$I_y\ddot{\theta} = M_y \tag{2}$$

$$m_1\left[\ddot{q}_1 + 2\zeta_1\omega_1\dot{q}_1 + \omega_1^2 q_1\right] = -Q_{1z} \tag{3}$$

$$m_2\left[\ddot{q}_2 + 2\zeta_2\omega_2\dot{q}_2 + \omega_2^2 q_2\right] = -Q_{2z} \tag{4}$$

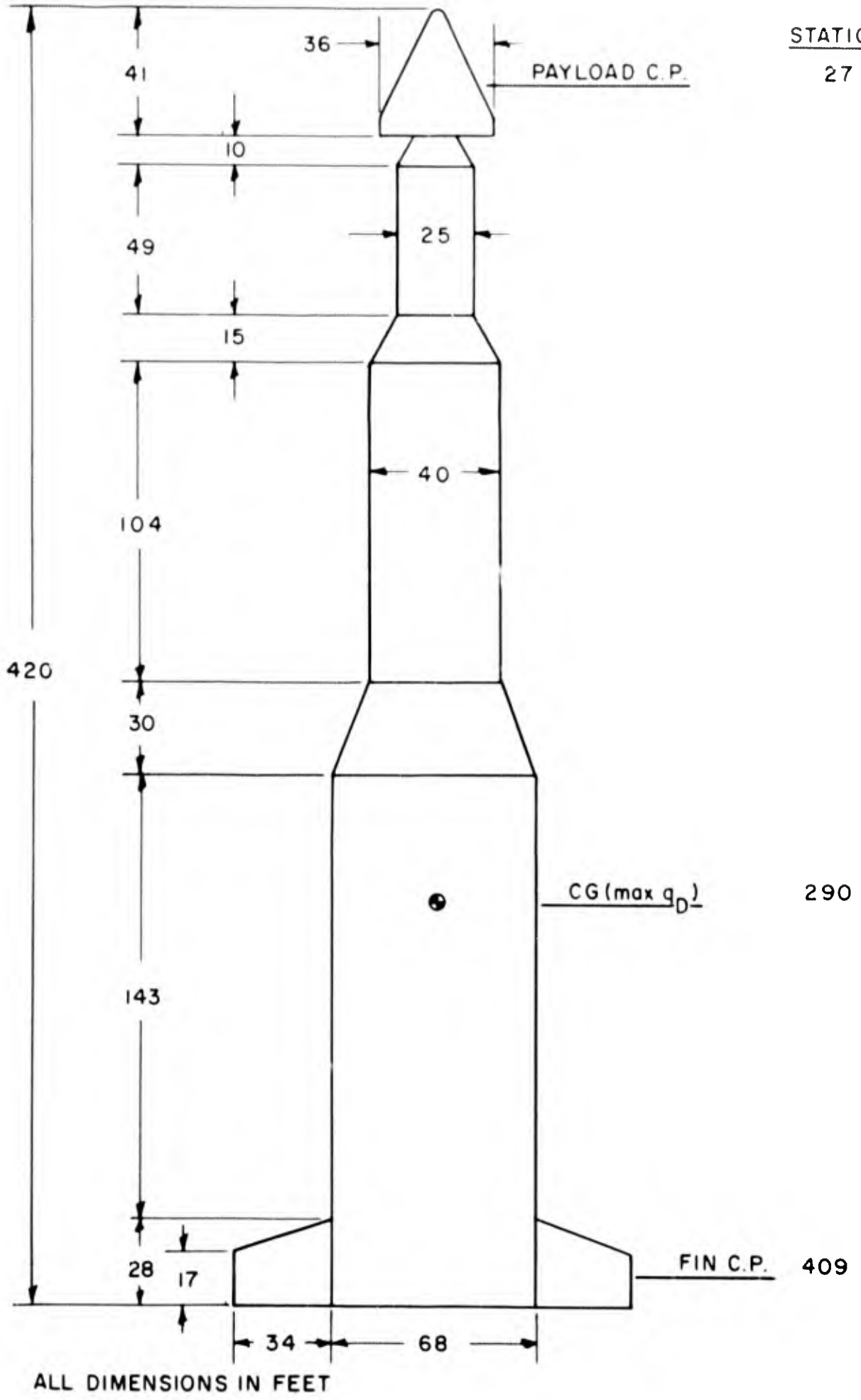

Figure 1. Basic Configuration

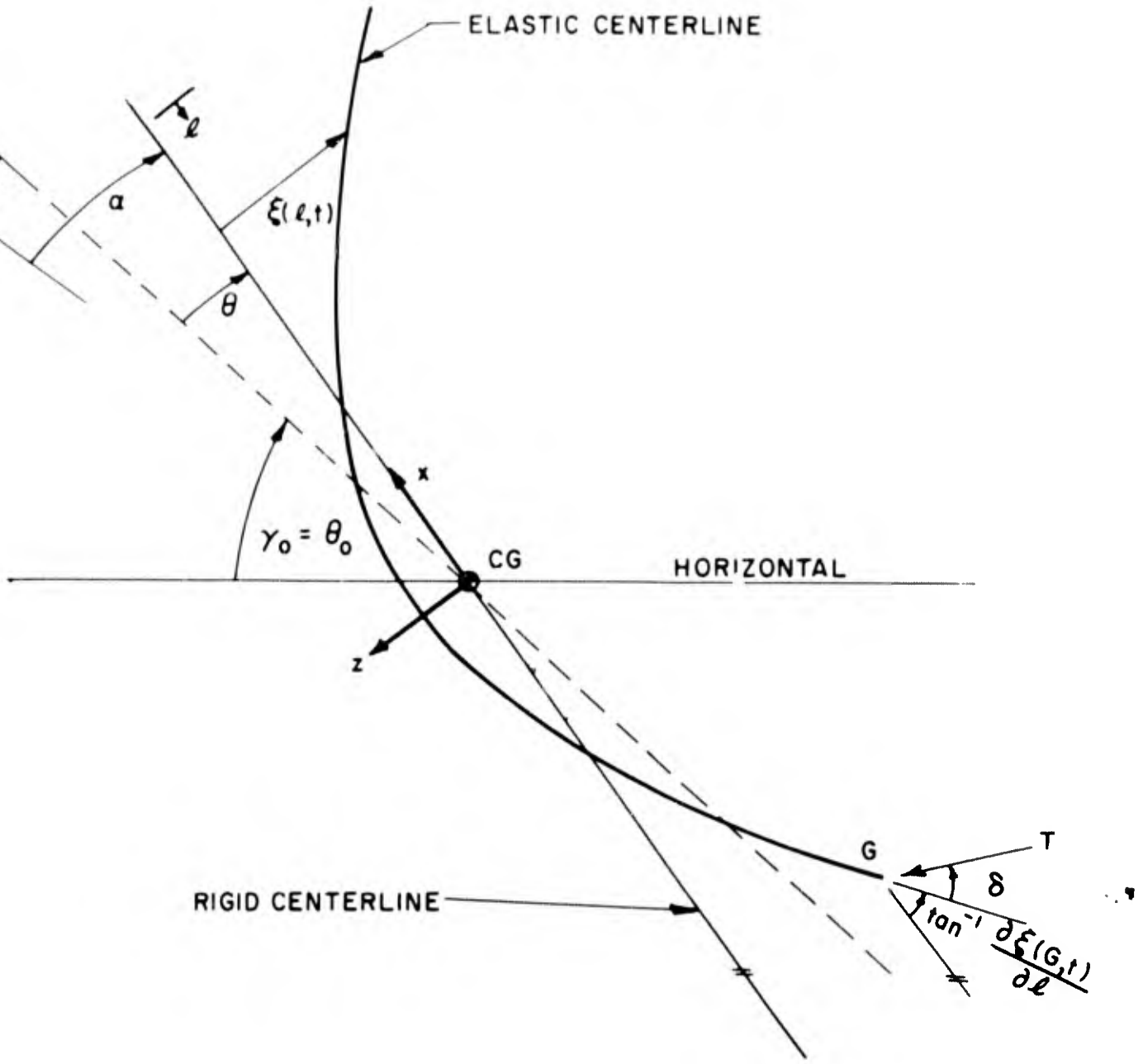

Figure 2. Schematic of Elastic Missile

The $(Mg\theta \sin\gamma_o)$ gravity term arises from the motion of the vehicle relative to an inertial reference system. It is commonly omitted for attitude stability studies for large boosters, since the effects of the flight path coupling into attitude stability (through aerodynamic force perturbations) are minor. Therefore, for simpliciation, it will be omitted in the equations to follow. F_z, M_y, Q_{1z}, and Q_{2z} are made up of thrust and aerodynamic terms:

$$F_z = F_T + F_A \tag{5}$$

$$M_y = M_T + M_A \tag{6}$$

$$Q_{1z} = Q_{1T} + Q_{1A} \tag{7}$$

$$Q_{2z} = Q_{2T} + Q_{2A} \tag{8}$$

Referring to Figure 2, it can be determined that

$$F_T = T\sin\left[\tan^{-1}\frac{\partial\xi(G,t)}{\partial\ell}\right] + T\sin\delta\ ; \tag{9}$$

and for small $\tan^{-1}\frac{\partial\xi(G,t)}{\partial\ell}$ and δ,

$$F_T \cong T\frac{\partial\xi(G,t)}{\partial\ell} + T\delta\ . \tag{10}$$

Also,

$$M_T \cong \ell_G T\frac{\partial\xi(G,t)}{\partial\ell} - \xi(G,t)T + T\ell_G\delta \tag{11}$$

$$Q_{1T} = F_T\phi_1(G) \cong \phi_1(G)T\frac{\partial\xi(G,t)}{\partial\ell} + T\phi_1(G)\delta \tag{12}$$

$$Q_{2T} = F_T\phi_2(G) \cong \phi_2(G)T\frac{\partial\xi(G,t)}{\partial\ell} + T\phi_2(G)\delta \tag{13}$$

where $\phi_1(G)$ and $\phi_2(G)$ are the normalized elastic mode deflections of the first and second modes at the point of thrust application. Assuming the flexibility to be represented adequately by the first and second elastic modes, the thrust forces and moments can be approximated reasonably by

$$F_T \cong T\frac{\partial\xi(G,t)}{\partial\ell} + T\delta \cong -T\left[\sigma_1(G)q_1 + \sigma_2(G)q_2 - \delta\right] \tag{14}$$

$$M_T \cong T\left[\ell_G \frac{\partial \xi(G,t)}{\partial \ell} - \xi(G,t) + \ell_G \delta\right] \cong -T\left[\ell_G \sigma_1(G) + \phi_1(G)\right] q_1$$

$$- T\left[\ell_G \sigma_2(G) + \phi_2(G)\right] q_2 + T\ell_G \delta \tag{15}$$

$$Q_{1T} \cong -T\left[\sigma_1(G)\phi_1(G) q_1 + \sigma_2(G)\phi_1(G) q_2\right] + T\phi_1(G)\delta \tag{16}$$

$$Q_{2T} \cong -T\left[\sigma_1(G)\phi_2(G) q_1 + \sigma_2(G)\phi_2(G) q_2\right] + T\phi_2(G)\delta \tag{17}$$

where

$$\xi(G,t) \cong \phi_1(G) q_1(t) + \phi_2(G) q_2(t) \tag{18}$$

and

$$\frac{\partial \xi(G,t)}{\partial \ell} \cong \frac{\partial \phi_1(G)}{\partial \ell} q_1(t) + \frac{\partial \phi_2(G)}{\partial \ell} q_2(t) = -\left[\sigma_1(G) q_1 + \sigma_2(G) q_2\right] . \tag{19}$$

From Equation 19 it is evident that $\sigma_1(G)$ and $\sigma_2(G)$ are the negative slopes of the normalized mode shapes at the point of thrust application. Explanations of the relationships between physical elastic deflections $\xi(\ell,t)$ and mode shapes, slopes, and generalized coordinates ϕ_1, ϕ_2, σ_1, σ_2, q_1, and q_2 can be found in References 1, 2, and 3.

Attention is next given to the derivation of the aerodynamic force and moment, F_A and M_A, and the generalized forces Q_{1A} and Q_{2A}. Assuming linear, quasi-steady aerodynamics,

$$F_A = -\frac{1}{2}\rho U^2 \int_0^L S_r \frac{\partial C_N(\ell)}{\partial \alpha} \bar{\alpha}(\ell)\, d\ell \tag{20}$$

where

$$\bar{\alpha}(\ell) = \alpha - \frac{(\ell_{CG} - \ell)}{U}\dot{\theta} - \frac{\partial \xi}{\partial \ell} - \frac{\dot{\xi}}{U} . \tag{21}$$

Therefore,

$$F_A = -\frac{1}{2}\rho U^2\Big[\alpha\int_0^L S_r\frac{\partial C_N(\ell)}{\partial\alpha}d\ell - \frac{\dot\theta}{U}\int_0^L S_r\frac{\partial C_N(\ell)}{\partial\alpha}(\ell_{CG}-\ell)d\ell$$

$$+ q_1\int_0^L S_r\frac{\partial C_N(\ell)}{\partial\alpha}\sigma_1(\ell)d\ell - \frac{\dot q_1}{U}\int_0^L S_r\frac{\partial C_N(\ell)}{\partial\alpha}\phi_1(\ell)d\ell + q_2\int_0^L S_r\frac{\partial C_N(\ell)}{\partial\alpha}\sigma_2(\ell)d\ell$$

$$- \frac{\dot q_2}{U}\int_0^L S_r\frac{\partial C_N(\ell)}{\partial\alpha}\phi_2(\ell)d\ell\Big] \qquad (22)$$

where, in general, the normal force curve slopes of the lifting-payload, booster body, and stabilizing fins will be based on different reference areas S_r.

The aerodynamic moment M_A is given by

$$M_A = \frac{1}{2}\rho U^2\int_0^L S_r\frac{\partial C_N(\ell)}{\partial\alpha}(\ell_{CG}-\ell)\bar\alpha(\ell)d\ell \qquad (23)$$

or

$$M_A = \frac{1}{2}\rho U^2\Big[\alpha\int_0^L S_r\frac{\partial C_N(\ell)}{\partial\alpha}(\ell_{CG}-\ell)d\ell - \frac{\dot\theta}{U}\int_0^L S_r\frac{\partial C_N(\ell)}{\partial\alpha}(\ell_{CG}-\ell)^2d\ell$$

$$+ q_1\int_0^L S_r\frac{\partial C_N(\ell)}{\partial\alpha}\sigma_1(\ell)(\ell_{CG}-\ell)d\ell - \frac{\dot q_1}{U}\int_0^L S_r\frac{\partial C_N(\ell)}{\partial\alpha}\phi_1(\ell)(\ell_{CG}-\ell)d\ell$$

$$+ q_2\int_0^L S_r\frac{\partial C_N(\ell)}{\partial\alpha}\sigma_2(\ell)(\ell_{CG}-\ell)d\ell - \frac{\dot q_2}{U}\int_0^L S_r\frac{\partial C_N(\ell)}{\partial\alpha}\phi_2(\ell)(\ell_{CG}-\ell)d\ell\Big]. \qquad (24)$$

The generalized aerodynamic forces Q_{1A} and Q_{2A} are given by

$$Q_{1A} = \int_0^L\frac{dF_A}{d\ell}\phi_1(\ell)d\ell = -\frac{1}{2}\rho U^2\int_0^L S_r\frac{\partial C_N(\ell)}{\partial\alpha}\phi_1(\ell)\bar\alpha(\ell)d\ell \qquad (25)$$

$$Q_{2A} = \int_0^L\frac{dF_A}{d\ell}\phi_2(\ell)d\ell = -\frac{1}{2}\rho U^2\int_0^L S_r\frac{\partial C_N(\ell)}{\partial\alpha}\phi_2(\ell)\bar\alpha(\ell)d\ell. \qquad (26)$$

Using Equations 18, 19, and 21, Equations 25 and 26 become

$$Q_{1A} = -\frac{1}{2}\rho U^2 \Big[\alpha \int_0^L S_r \frac{\partial C_N(\ell)}{\partial \alpha} \phi_1(\ell)\, d\ell - \frac{\dot{\theta}}{U} \int_0^L S_r \frac{\partial C_N(\ell)}{\partial \alpha} \phi_1(\ell)(\ell_{CG} - \ell)\, d\ell$$

$$+ q_1 \int_0^L S_r \frac{\partial C_N(\ell)}{\partial \alpha} \sigma_1(\ell)\phi_1(\ell)\, d\ell - \frac{\dot{q}_1}{U} \int_0^L S_r \frac{\partial C_N(\ell)}{\partial \alpha} \phi_1^2(\ell)\, d\ell$$

$$+ q_2 \int_0^L S_r \frac{\partial C_N(\ell)}{\partial \alpha} \sigma_2(\ell)\phi_1(\ell)\, d\ell - \frac{\dot{q}_2}{U} \int_0^L S_r \frac{\partial C_N(\ell)}{\partial \alpha} \phi_1(\ell)\phi_2(\ell)\, d\ell \Big]; \qquad (27)$$

$$Q_{2A} = -\frac{1}{2}\rho U^2 \Big[\alpha \int_0^L S_r \frac{\partial C_N(\ell)}{\partial \alpha} \phi_2(\ell)\, d\ell - \frac{\dot{\theta}}{U} \int_0^L S_r \frac{\partial C_N(\ell)}{\partial \alpha} \phi_2(\ell)(\ell_{CG} - \ell)\, d\ell$$

$$+ q_1 \int_0^L S_r \frac{\partial C_N(\ell)}{\partial \alpha} \sigma_1(\ell)\phi_2(\ell)\, d\ell - \frac{\dot{q}_1}{U} \int_0^L S_r \frac{\partial C_N(\ell)}{\partial \alpha} \phi_1(\ell)\phi_2(\ell)\, d\ell$$

$$+ q_2 \int_0^L S_r \frac{\partial C_N(\ell)}{\partial \alpha} \sigma_2(\ell)\phi_2(\ell)\, d\ell - \frac{\dot{q}_2}{U} \int_0^L S_r \frac{\partial C_N(\ell)}{\partial \alpha} \phi_2^2(\ell)\, d\ell \Big]. \qquad (28)$$

As mentioned above, the reference areas for the normal force curve slopes of the lifting-payload, booster body, and fins are, in general, different; however, in this analysis the normal force curve slopes at each station along the entire vehicle are based on the total vehicle planform area S.

The complete equations of motion describing the vehicle transient response to control and gust inputs are obtained by incorporating Equations 14, 15, 16, 17, 22, 24, 27, and 28 into Equations 1, 2, 3, and 4 and collecting terms. Application of the Laplace transformation for zero initial conditions results in the matrix of equations given below, Equation 29. The column matrix in α_g represents forcing functions due to gust and wind shear disturbances which the vehicle encounters during boost. The induced angle of attack history α_g can be obtained by combining known wind shear profiles with known nominal trajectory parameters.

$$\begin{bmatrix} (U s + Z_\alpha)(Z_\theta - U)s & (Z_{\dot{q}_1} s + Z_{q_1}) & (Z_{\dot{q}_2} s + Z_{q_2}) \\ M_\alpha & (s^2 + M_\theta s) & (M_{\dot{q}_1} s + M_{q_1}) & (M_{\dot{q}_2} s + M_{q_2}) \\ F_{1\alpha} & F_{1\theta} s & (s^2 + F_{1\dot{q}_1} s + F_{1q_1})(F_{1\dot{q}_2} s + F_{1q_2}) \\ F_{2\alpha} & F_{2\theta} s & (F_{2\dot{q}_1} s + F_{2q_1}) & (s^2 + F_{2\dot{q}_2} s + F_{2q_2}) \end{bmatrix} \begin{Bmatrix} \alpha(s) \\ \theta(s) \\ q_1(s) \\ q_2(s) \end{Bmatrix} = \begin{Bmatrix} -Z_\delta \\ -M_\delta \\ -F_{1\delta} \\ -F_{2\delta} \end{Bmatrix} \delta(s) + \begin{Bmatrix} -Z_\alpha \\ -M_\alpha \\ -F_{1\alpha} \\ -F_{2\alpha} \end{Bmatrix} \alpha_g(s). \quad (29)$$

The coefficients in matrix Equation 29 are defined below.

$$Z_\alpha = \frac{q_D S}{M} \int_0^L C_{N_\alpha} d\ell$$

$$M_\alpha = -\frac{q_D S}{I_y} \int_0^L C_{N_\alpha} (\ell_{CG} - \ell) d\ell$$

$$F_{1\alpha} = -\frac{q_D S}{m_1} \int_0^L C_{N_\alpha} \phi_1 d\ell$$

$$F_{2\alpha} = -\frac{q_D S}{m_2} \int_0^L C_{N_\alpha} \phi_2 d\ell$$

$$Z_\theta = -\frac{q_D S}{MU} \int_0^L C_{N_\alpha} (\ell_{CG} - \ell) d\ell$$

$$M_\theta = \frac{q_D S}{I_y U} \int_0^L C_{N_\alpha} (\ell_{CG} - \ell)^2 d\ell$$

$$F_{1\theta} = \frac{q_D S}{m_1 U} \int_0^L C_{N_\alpha} \phi_1 (\ell_{CG} - \ell) d\ell$$

$$F_{2\theta} = \frac{q_D S}{m_2 U} \int_0^L C_{N_\alpha} \phi_2 (\ell_{CG} - \ell) d\ell$$

$$Z_{\dot{q}_1} = -\frac{q_D S}{MU} \int_0^L C_{N_\alpha} \phi_1 \, d\ell$$

$$Z_{q_1} = \frac{q_D S}{M} \int_0^L C_{N_\alpha} \sigma_1 \, d\ell + \frac{T}{M} \sigma_1 (G)$$

$$M_{\dot{q}_1} = \frac{q_D S}{I_y U} \int_0^L C_{N_\alpha} \phi_1 (\ell_{CG} - \ell) \, d\ell$$

$$M_{q_1} = \frac{T}{I_y} \left[\ell_G \sigma_1 (G) + \phi_1 (G) \right] - \frac{q_D S}{I_y} \int_0^L C_{N_\alpha} \sigma_1 (\ell_{CG} - \ell) \, d\ell$$

$$F_{1\dot{q}_1} = 2\zeta_1 \omega_1 + \frac{q_D S}{m_1 U} \int_0^L C_{N_\alpha} \phi_1^2 \, d\ell$$

$$F_{1q_1} = \omega_1^2 - \frac{T}{m_1} \sigma_1 (G) \phi_1 (G) - \frac{q_D S}{m_1} \int_0^L C_{N_\alpha} \sigma_1 \phi_1 \, d\ell$$

$$F_{2\dot{q}_1} = \frac{q_D S}{m_2 U} \int_0^L C_{N_\alpha} \phi_1 \phi_2 \, d\ell$$

$$F_{2q_1} = -\frac{q_D S}{m_2} \int_0^L C_{N_\alpha} \sigma_1 \phi_2 \, d\ell - \frac{T}{m_2} \sigma_1 (G) \phi_2 (G)$$

$$Z_{\dot{q}_2} = -\frac{q_D S}{MU} \int_0^L C_{N_\alpha} \phi_2 \, d\ell$$

$$Z_{q_2} = \frac{q_D S}{M} \int_0^L C_{N_\alpha} \sigma_2 \, d\ell + \frac{T}{M} \sigma_2 (G)$$

$$M_{\dot{q}_2} = \frac{q_D S}{I_y U} \int_0^L C_{N_\alpha} \phi_2 (\ell_{CG} - \ell) \, d\ell$$

$$M_{q_2} = \frac{T}{I_y} \left[\ell_G \sigma_2 (G) + \phi_2 (G) \right] - \frac{q_D S}{I_y} \int_0^L C_{N_\alpha} \sigma_2 (\ell_{CG} - \ell) \, d\ell$$

$$F_{1\dot{q}_2} = \frac{q_D S}{m_1 U} \int_0^L C_{N_\alpha} \phi_1 \phi_2 \, d\ell$$

$$F_{1q_2} = -\frac{q_D S}{m_1}\int_0^L C_{N_\alpha}\,\sigma_2\,\phi_1\,d\ell - \frac{T}{m_1}\,\sigma_2(G)\,\phi_1(G)$$

$$F_{2\dot{q}_2} = 2\zeta_2\omega_2 + \frac{q_D S}{m_2 U}\int_0^L C_{N_\alpha}\,\phi_2^{\,2}\,d\ell$$

$$F_{2q_2} = \omega_2^{\,2} - \frac{T}{m_2}\,\sigma_2(G)\,\phi_2(G) - \frac{q_D S}{m_2}\int_0^L C_{N_\alpha}\,\sigma_2\,\phi_2\,d\ell$$

$$Z_\delta = -\frac{T}{M}$$

$$M_\delta = -\frac{T\ell_G}{I_y}$$

$$F_{1\delta} = \frac{T}{m_1}\,\phi_1(G)$$

$$F_{2\delta} = \frac{T}{m_2}\,\phi_2(G)$$

SECTION II

TRAJECTORY EQUATIONS AND ELASTIC CHARACTERISTICS

For the present purpose an approximation to the trajectory is adequate. So, neglecting aerodynamic drag, the acceleration a_o tangent to the nominal flight path γ_o is given by

$$a_o \cong \frac{T}{M} - g \sin\gamma_o = \frac{T}{M_o - m_p t} - g \sin\gamma_o \tag{30}$$

where M_o is the total launch mass and m_p is the propellant flow or burning rate. The steady-state, forward flight velocity tangent to the flight path is

$$U = \int_0^t a_o d\tau = T\int_0^t (M_o - m_p\tau)^{-1} d\tau - g\int_0^t \sin\gamma_o \, d\tau \ . \tag{31}$$

Integration yields

$$U \cong \frac{T}{m_p} \ln \frac{M_o}{M} - gt\,\overline{\sin\gamma_o} \tag{32}$$

Where

$$\overline{\sin\gamma_o} = \frac{1}{t}\int_0^t \sin\gamma_o \, d\tau \ . \tag{33}$$

To obtain altitude as a function of time, one has, to an approximation,

$$h \cong \int_0^t \frac{T}{m_p} (\sin\gamma_o) \ln \frac{M_o}{M} d\tau - g\,\overline{\sin\gamma_o}\int_0^t \tau \sin\gamma_o \, d\tau \tag{34}$$

or,

$$h \cong \frac{T\overline{\sin\gamma_o}}{m_p}\left[\int_0^t \ln M_o \, d\tau - \int_0^t \ln(M_o - m_p\tau)\, d\tau\right] - \frac{1}{2} gt^2 (\overline{\sin\gamma_o})^2 \ . \tag{35}$$

Integrating,

$$h \cong \frac{T\overline{\sin\gamma_0}}{m_p}\left\{t \ln M_0 + \left[\frac{M_0}{m_p} - t\right]\left[\ln(M_0 - m_p t) - 1\right] - \frac{M_0}{m_p}(\ln M_0 - 1)\right\} - \frac{1}{2} g t^2 (\overline{\sin\gamma_0})^2 \quad (36)$$

which becomes

$$h \cong -\frac{1}{2} g t^2 (\overline{\sin\gamma_0})^2 + \frac{T\overline{\sin\gamma_0}}{m_p}\left\{\left[1 + \ln\frac{M_0}{(M_0 - m_p t)}\right] t + \frac{M_0}{m_p}\left[\ln\left(1 - \frac{m_p t}{M_0}\right)\right]\right\}. \quad (37)$$

Upon selecting the trajectory γ_0 as a function of time, Equations 30, 32, and 37 can be used to determine a_0, U, and h, as functions of time. Knowledge of h implies knowledge of the air density ρ ; therefore, the dynamic pressure q_D can be determined as a function of time.

A total launch weight $M_0 g$ of 8×10^6 lbs is assumed for the configuration of Figure 1. The first stage burning time is taken as 110 seconds with the first stage burnout weight being 2×10^6 lbs. Assuming a constant propellant burning rate, the mass flow rate m_p is determined to be 1690 slugs/sec. A constant thrust T of 12.26×10^6 lbs is used.

The above data are used in Equations 32 and 37 to calculate time histories of U and h. These velocity and altitude histories are then used to determine the dynamic pressure time history. These trajectory parameters are plotted in Figures 3 and 4. It can be seen from Figure 3 that the maximum dynamic pressure $q_{D_{max}}$ is 1340 lbs/ft^2 and occurs at t = 57.5 seconds. From Figure 4 this corresponds to U = 1860 ft/sec and occurs at h = 35,800 ft as shown on Figure 3.

Since the most serious dynamic stability problems nearly always occur at the maximum dynamic pressure flight condition, the analyses in this report is restricted to this flight condition. If the problem of providing active control of the elastic modes can be handled at this condition, it certainly can be successfully applied at flight conditions of reduced aerodynamic loading.

The payload for the configuration of Figure 1 is to be a 200,000-lb lifting reentry vehicle.

The aerodynamic force acting normal to the booster longitudinal axis due to a perturbation angle of attack α off the nominal ballistic trajectory consists of major components acting at the center of pressure of the lifting payload and the center of pressure of the booster stabilizing fins. The lift forces distributed along the booster body are small compared to these two major components and for simplicity will be neglected in the analysis. Typical values of the normal force derivative $\frac{\partial C_N(2)}{\partial \alpha}$ are taken at the $q_{D_{max}}$ condition to be

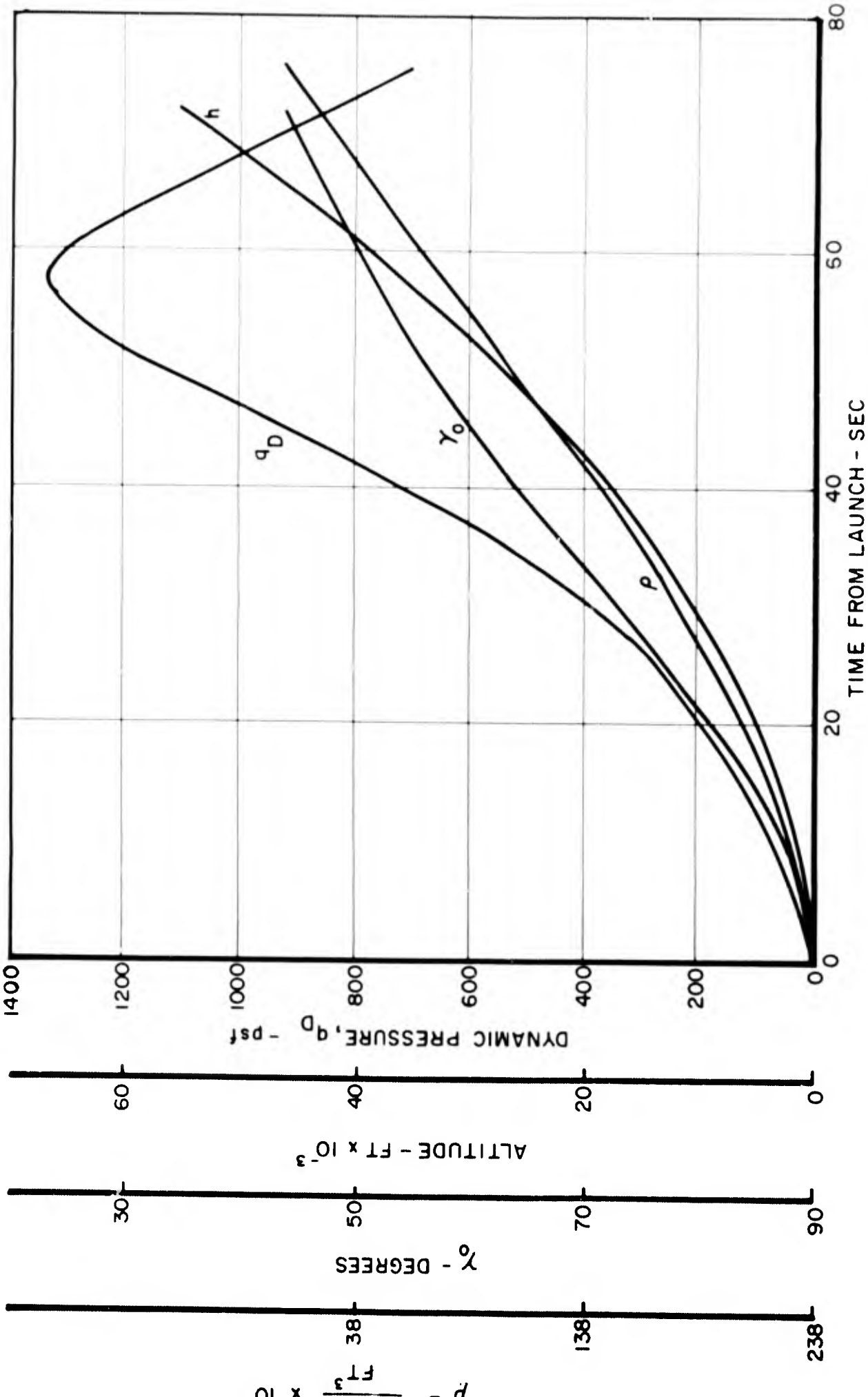

Figure 3. Trajectory Parameters

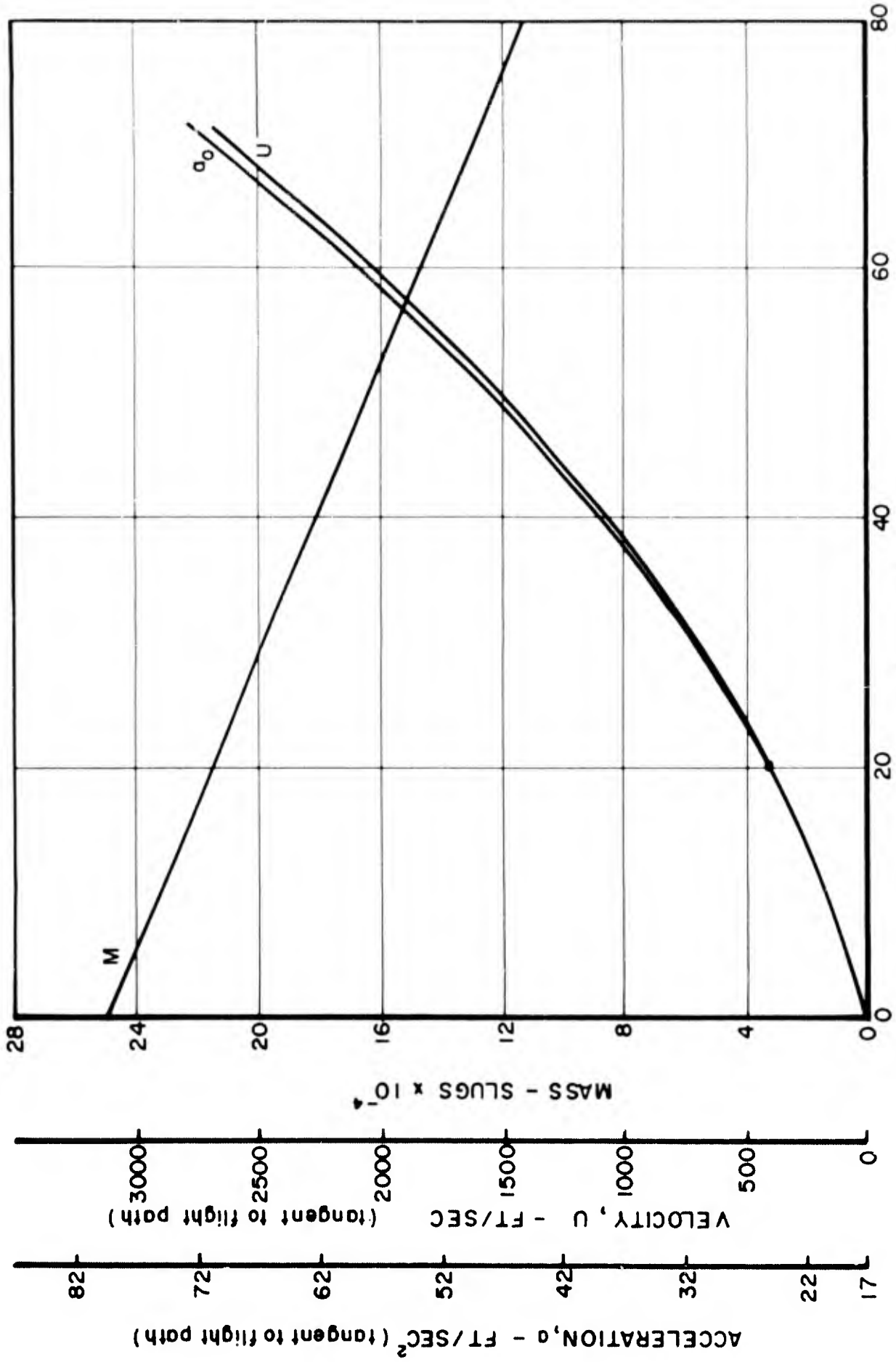

Figure 4. Trajectory Parameters

$$\frac{\partial C_N(\ell)}{\partial \alpha} \equiv C_{N_\alpha}(\ell) = 0.065$$ for the payload component and for the

$$\frac{\partial C_N(\ell)}{\partial \alpha} \equiv C_{N_\alpha}(\ell) = 0.196$$

stabilizing fins component. These values are based on the total vehicle planform area of 22,279 ft^2.

Turning now to the elastic characteristics of the vehicle, the assumed mass distribution is represented with concentrated masses at eleven stations along the axis. This distribution is shown in Table 1 and represents the distribution at the maximum dynamic pressure flight condition. With this distribution, the center of gravity is at station 290, and the total pitch mass moment of inertia about the CG is $I_y = 15.297 \times 10^8$ slugs-ft^2.

TABLE 1

MASS DATA

STATION (ft)	m (slugs)	$(\ell_{CG} - \ell)$ (ft)	I_y (slugs - ft^2)
27	6220	263	4.290×10^8
65	2553	225	1.290×10^8
103	2553	187	$.890 \times 10^8$
141	7600	149	1.685×10^8
179	7600	111	$.935 \times 10^8$
217	7600	73	$.404 \times 10^8$
255	22,435	35	$.275 \times 10^8$
293	22,435	-3	$.002 \times 10^8$
331	22,435	-41	$.376 \times 10^8$
369	22,435	-79	1.400×10^8
407	27,435	-117	3.750×10^8
	Total M = 151,300		Total Iy = 15.297×10^8

Figure 5 shows the first and second normalized elastic mode shapes to be used in this analysis. They are assumed shapes based on the assumed mass distribution, and they satisfy the following necessary equilibrium conditions:

$$\sum_{i=1}^{11} m^{(i)} \phi_1^{(i)} = 0 \; ; \quad \sum_{i=1}^{11} m^{(i)} \phi_2^{(i)} = 0 \; ; \quad \sum_{i=1}^{11} m^{(i)} \phi_1^{(i)} \phi_2^{(i)} = 0 ,$$

where i = 1,2,3,.....,11 are the mass stations. Other first and second mode shapes which satisfy these equilibrium conditions are possible. In order to arrive at unique modes, the stiffness distribution EI must be specified along the vehicle axis. The only specification to be put on the stiffness in this analysis is that undamped first and second elastic mode natural frequencies are ω_1 = 1 rad/sec and ω_2 = 3 rad/sec. With no further information on stiffness, the modes of Figure 5 represent typical but not unique first and second elastic modes. Typical shapes are sufficient for purposes here. Table 2 is a tabulation of the modal data from Figure 5. As will be seen later, the above value for ω_1 is of the same order of magnitude as the booster's uncoupled, short-period frequency and gives rise to a severe mode interaction problem.

All the data are now available to calculate the coefficients of Equation 29. The transient dynamics resulting from the determinant of the square matrix of coefficients in Equation 29 will be examined in the next section.

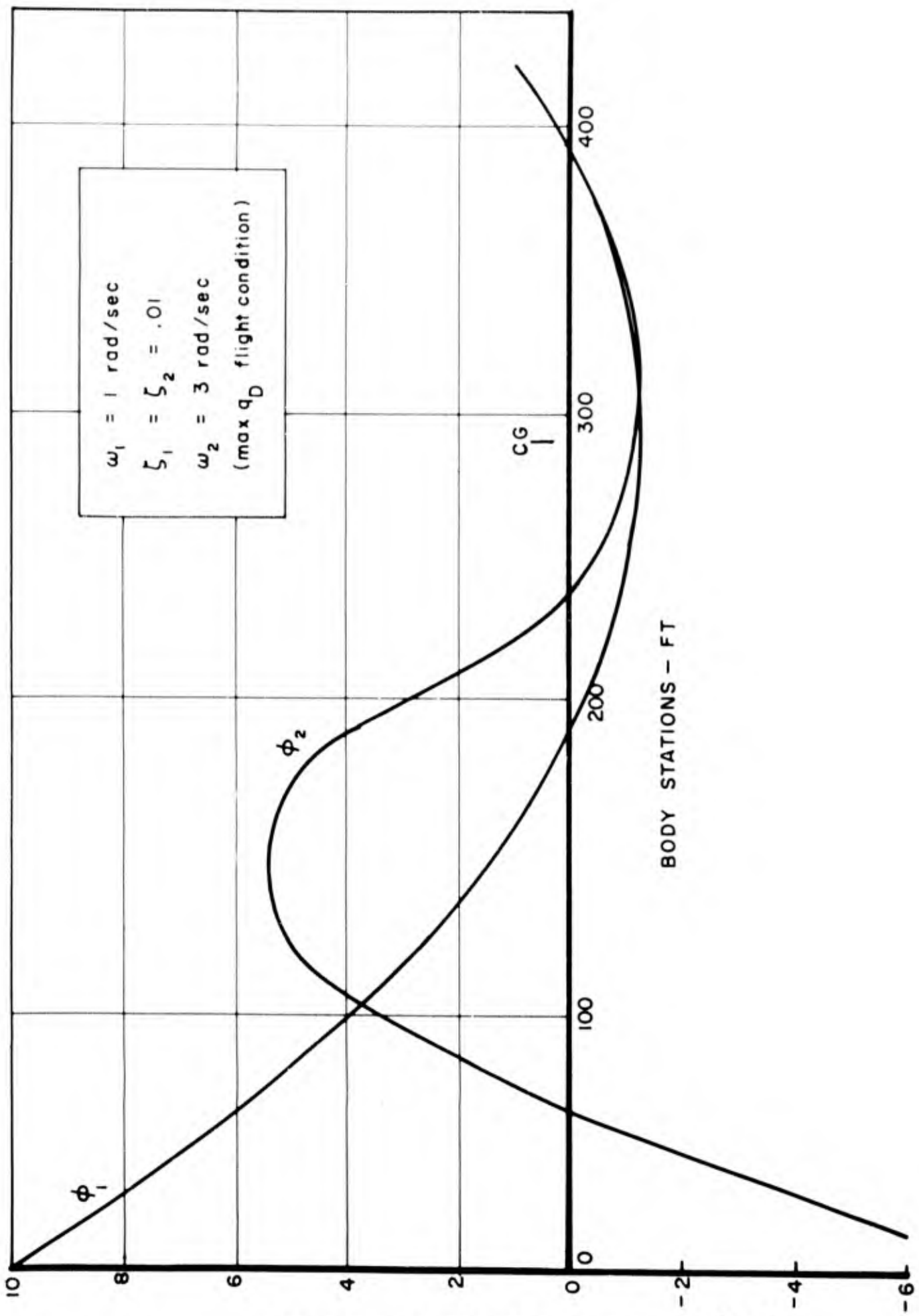

Figure 5. First and Second Elastic Modes

TABLE 2

MODE SHAPE DATA

STATION (ft)	ϕ_1	ϕ_2	$m\phi_1^2$ (slugs)	$m\phi_2^2$ (slugs)	σ_1 $\left(\frac{1}{ft}\right)$	σ_2 $\left(\frac{1}{ft}\right)$
27	8.00	-4.00	398,000	99,500	.0739	-.1575
65	5.40	1.00	74,400	2,553	NOT USED	NOT USED
103	3.25	4.50	26,930	51,650		
141	1.55	5.40	18,230	221,500		
179	.25	4.60	475	160,700		
217	-.62	1.30	2,920	12,840		
255	-1.08	-.65	26,150	9,480		
293	-1.23	-1.20	34,000	32,300		
331	-1.10	-1.20	27,170	32,300		
369	-.60	-.65	8,080	9,480		
407	.45	.40	5,560	4,390	-.0407	-.0407
			Total m_1 = 621,915	m_2 = 636,693		

$\phi_1(G) = \phi_2(G) = 1$

$\sigma_1(G) = \sigma_2(G) = -.05 \frac{1}{ft}$

SECTION III

FORWARD-LOOP TRANSIENT DYNAMICS

Using the data presented in Section II, the coefficients can be calculated, and Equation 29 becomes

$$\left[\begin{array}{cc|c} (1860s + 51.6) & -1859s & \\ .1143 & (s^2 + .0755s) & \\ \hline -29.3 & 3.27s & \\ 8.55 & -1.96s & \end{array}\right]$$

$$\left[\begin{array}{cc} (-.0647s - 4.682) & (.01933s - 7.66) \\ (.001326s - .087) & (-.000815s - .0097) \\ \hline (s^2 + .1285s + .312) & (-.0482s + 5.107) \\ (-.05175s + 2.013) & (s^2 + .087s + 8.181) \end{array}\right] \left\{\begin{array}{c} \alpha(s) \\ \theta(s) \\ \hline q_1(s) \\ q_2(s) \end{array}\right\} = \left\{\begin{array}{c} 81 \\ 1.042 \\ \hline -19.72 \\ -19.25 \end{array}\right\} \delta(s) + \left\{\begin{array}{c} -51.6 \\ -.1143 \\ \hline 29.3 \\ -8.55 \end{array}\right\} \alpha_g(s) \qquad (38)$$

The terms coupling the elastic modes and rigid-body equations are located in the upper right and lower left quadrants of the partitioned square matrix. Expansion of the determinant in the upper left quadrant gives the uncoupled, rigid-body-only, short-period transient dynamics:

$$s(s^2 + .1032s + .1164) = s(s^2 + 2\zeta_{sp}\omega_{sp}s + \omega_{sp}^2) = 0. \qquad (39)$$

Solving Equation 39 for ω_{sp} and ζ_{sp} gives

$$\omega_{sp} = .342 \frac{rad}{sec} \quad \text{and} \quad \zeta_{sp} = .151 .$$

Now, the effects of including the first elastic mode will be examined. An IBM 7094 digital program is used to expand and factor the 3 X 3 determinant. It yields the following polynomial equation:

$$(s - 1.08)(s + 1.28)(s^2 + .0387s + 1.813) = (s - \frac{1}{T_{1sp}})(s - \frac{1}{T_{2sp}})(s^2 + 2\zeta_{1e}\omega_{1e}s + \omega_{1e}^2) = 0. \qquad (40)$$

From Equation 40 one sees the first quantitative evidence of the effects produced by mode interaction. The quadratic which corresponds to the short-period mode consists of two real roots instead of the conventional complex pair. One of these real roots is positive, indicating that the interaction has caused the vehicle to exhibit a rigid-body divergence; that is, a divergence of the pitch angle θ. This of course, is intolerable; and one of the tasks of the automatic control system, to be considered in a later section, will be to eliminate this divergence and restore acceptable short-period dynamics. The elastic mode quadratic in Equation 40 yields a coupled first elastic mode undamped frequency $\omega_{1e} = 1.347$ rad/sec and a damping ratio $\zeta_{1e} = .014$, which are close to the uncoupled values of $\omega_1 = 1$ rad/sec and $\zeta_1 = .01$. Thus, nearly all the adverse effects of the interaction are on the rigid-body motion; this will not always be the case, as will be seen later.

By adding the second elastic mode to the system, expansion and factorization of the 4 x 4 determinant yields

$$(s - 1.31)(s + 1.54)(s^2 + .0236s + 1.323)(s^2 + .0615s + 9.3) =$$

$$(s - \frac{1}{T_{1sp}})(s - \frac{1}{T_{2sp}})(s^2 + 2\zeta_{1e}\omega_{1e}s + \omega_{1e}^2)(s^2 + 2\zeta_{2e}\omega_{2e}s + \omega_{2e}^2) = 0. \qquad (41)$$

It is seen from Equation 41 that the addition of the second elastic mode has not changed the basic character of the interaction. There is still the rigid-body divergence, and the coupled elastic modes' undamped frequencies and damping ratios are

$$\omega_{1e} = 1.15 \frac{rad}{sec}; \qquad \zeta_{1e} = .01$$

$$\omega_{2e} = 3.05 \frac{rad}{sec}; \qquad \zeta_{2e} = .01.$$

It would be useful to see if the term or terms in the equations of motion responsible for the severe interaction between rigid-body and elastic motion can be uncovered. To further simplify the analysis but without losing the essence of the problem, consider only the three-degree-of-freedom system made up of the two rigid-body equations and the first elastic mode. The characteristic stability determinant of this system taken from Equation 38 is

$$\begin{vmatrix} (1860s + 51.6) & -1859s & (-.0647s - 4.682) \\ .1143 & (s^2 + .0755s) & (.001326s - .087) \\ -29.3 & 3.27s & (s^2 + .1285s + .312) \end{vmatrix} = 0. \qquad (42)$$

Equation 42 can be expanded as follows:

$$(s^2 + .1285s + .312) \begin{vmatrix} (1860s + 51.6) & -1859s \\ .1143 & (s^2 + .0755s) \end{vmatrix}$$

$$-3.27s \begin{vmatrix} (1860s + 51.6) & (-.0647s - 4.682) \\ .1143 & (.001326s - .087) \end{vmatrix}$$

$$-29.3 \begin{vmatrix} -1859s & (-.0647s - 4.682) \\ (s^2 + .0755s) & (.001326s - .087) \end{vmatrix} = 0. \qquad (43)$$

All the terms contributing to the mode interaction (coupling) are contained in the last two of the three determinant products of Equation 43. By referring to Equation 29 and the literal expressions at the conclusion of Section I, it can be seen that the only elastic parameters occurring in these two determinant products are mode deflections and slopes; the elastic mode undamped natural frequency ω_1 and structural damping ratio ζ_1 appear only in the first determinant product of Equation 43. It is obvious that if the sum of these two determinant products can be made zero, then the transient dynamics would be determined by

$$(s^2 + .1285s + .312) \begin{vmatrix} (1860s + 51.6) & -1859s \\ .1143 & (s^2 + .0755s) \end{vmatrix} = 0. \qquad (44)$$

The 2 x 2 determinant in Equation 44 contains the uncoupled, short-period quadratic and is completely independent of the elastic properties. In literal terms, the coefficients of the elastic quadratic are

$$.1285 = 2\zeta_{1e}\omega_{1e} = 2\zeta_1\omega_1 + \frac{q_D S}{m_1 U}\int_0^L C_{N_\alpha}\phi_1^2\, d\ell \qquad (45)$$

$$.312 = \omega_{1e}^2 = \omega_1^2 - \frac{q_D S}{m_1}\int_0^L C_{N_\alpha}\sigma_1\phi_1\, d\ell - \frac{T}{m_1}\phi_1(G)\sigma_1(G)\,. \qquad (46)$$

All the terms of Equation 45 are positive since the only values of C_{N_α} of significance occur at the lifting-payload center of pressure and stabilizing fins centers of pressure, and both are positive. The first elastic mode must, therefore, always be positively damped when the coupling terms are zero. Furthermore

$$\zeta_{1e} \geq \zeta_1 \frac{\omega_1}{\omega_{1e}} .$$

Ideally, one would like to have

$$-3.27s \begin{vmatrix} (1860s + 51.6) & (-.0647s - 4.682) \\ .1143 & (.001326s - .087) \end{vmatrix}$$

$$-29.3 \begin{vmatrix} -1859s & (-.0647s - 4.682) \\ (s^2 + .0755s) & (.001326s - .087) \end{vmatrix} = 0. \qquad (47)$$

Expanding the determinants,

$$-\left[(3.27)(.001326)(1860) + (-29.3)(-.0647)\right]s^3 - \left[(3.27)(.001326)(51.6)\right.$$

$$+ (3.27)(-.087)(1860) - (3.27)(-.0647)(.1143) - (-29.3)(.001326)(-1859)$$

$$\left. + (-29.3)(-4.682) + (-29.3)(-.0647)(.0755)\right]s^2 - \left[(3.27)(-.087)(51.6)\right.$$

$$\left. -(3.27)(-4.682)(.1143) - (-29.3)(-.087)(-1859) + (-29.3)(-4.682)(.0755)\right]s = 0 \qquad (48)$$

where negligible terms have been lined out in Equation 48. Since the roots of the characteristic equation (Equation 43) are also dependent on the uncoupled elements, the only way for Equation 48 to hold is to have all coefficients of powers of s equal zero. Consider the uncoupled terms of Equation 43,

$$(s^2 + .1285s + .312) \begin{vmatrix} (1860s + 51.6) & -1859s \\ .1143 & (s^2 + .0755s) \end{vmatrix} . \qquad (49)$$

Expanding in powers of s gives

$$s^5 + .2317s^4 + .4417s^3 + .0472s^2 + .0363s \,. \tag{50}$$

Now, multiplying out the terms in Equation 48 gives

$$-9.94s^3 + 463s^2 - 4730s \,. \tag{51}$$

Comparing like powers in expressions 50 and 51, it is seen that the s^3, s^2, and s terms of expression 50 are negligible compared to those of expression 51. This indicates the dominate role played by the coupling terms in Equation 43. If the elastic mode undamped natural frequency had been at least an order of magnitude greater than the short-period frequency, the reverse would be true; that is, the coupling terms would be negligible, and there would be no instabilities due to mode interaction.

Writing the coefficients of Equation 48 or expression 51 in terms of the literal expressions defined at the conclusion of Section I, gives

$$\left\{-\frac{q_D^2 S^2}{I_y m_1 U}\left[\int_0^L C_{N_\alpha}\phi_1(\ell_{CG}-\ell)\,d\ell\right]^2 - \frac{q_D^2 S^2}{M m_1 U}\left[\int_0^L C_{N_\alpha}\phi_1\,d\ell\right]^2\right\} s^3$$

$$+\left\{\frac{q_D^2 S^2}{I_y m_1}\left[\int_0^L C_{N_\alpha}\phi_1(\ell_{CG}-\ell)\,d\ell\right]\left[\int_0^L C_{N_\alpha}\sigma_1(\ell_{CG}-\ell)\,d\ell - \frac{T}{q_D S}(\ell_G\sigma_1(G)+\phi_1(G))\right]\right.$$

$$+\frac{q_D^2 S^2}{M m_1}\left[\int_0^L C_{N_\alpha}\phi_1\,d\ell\right]\left[\int_0^L C_{N_\alpha}\sigma_1\,d\ell + \frac{T}{q_D S}\sigma_1(G)\right]$$

$$\left.+\frac{q_D^2 S^2}{I_y m_1 U}\left[\int_0^L C_{N_\alpha}\phi_1\,d\ell\right]\left[\int_0^L C_{N_\alpha}\phi_1(\ell_{CG}-\ell)\,d\ell\right]\left[U+\frac{q_D S}{MU}\int_0^L C_{N_\alpha}(\ell_{CG}-\ell)\,d\ell\right]\right\} s^2$$

$$+\left\{\frac{q_D S}{m_1}\left[\int_0^L C_{N_\alpha}\phi_1\,d\ell\right]\left[-\frac{q_D S}{I_y}\int_0^L C_{N_\alpha}\sigma_1(\ell_{CG}-\ell)\,d\ell + \frac{T}{I_y}(\ell_G\sigma_1(G)\right.\right.$$

$$\left.\left.+\phi_1(G))\right]\left[U+\frac{q_D S}{MU}\int_0^L C_{N_\alpha}(\ell_{CG}-\ell)\,d\ell\right]\right\} s. \tag{52}$$

An examination of expression 52 reveals that if the equations

$$\int_0^L C_{N_\alpha} \phi_1 \, d\ell = 0 \tag{53}$$

and

$$\int_0^L C_{N_\alpha} \phi_1 \ell \, d\ell = 0 \tag{54}$$

can be satisfied, then the coupling terms will all be zero. Unfortunately, it is not possible to satisfy both equations simultaneously. Assume that by a suitable choice of parameter values Equation 53 can be satisfied; then the values of $C_{N_\alpha}\phi_1$ at the lifting-payload and stabilizing fins centers of pressure must be equal but opposite in sign. In order for Equation 54 to be satisfied under these conditions, the distances from the nose to the centers of pressure of the payload and fins must be equal - but this is clearly impossible. Thus it is concluded that no simple configuration modification can be made to eliminate the coupling terms producing the mode interaction instabilities.

SECTION IV

CLOSED-LOOP TRANSIENT DYNAMICS

It was shown in the previous section that the mode interaction phenomenon has a profoundly unfavorable effect on the transient dynamics of the forward-loop. In this section an investigation will be made to see what influence the interaction has on transient dynamics when stability augmentation is provided by closing the loop with a simple feedback control to the thrust vector.

Let the control system consist of an actuator with a first-order lag, an ideal amplifier of gain K_A, an ideal pitch rate gyro of gain K_R, and an ideal pitch attitude gyro of unity gain. This degree of simplification is typical for a "first cut" at synthesis of an automatic flight control system. The system block diagram is shown in Figure 6 from which it can be determined that

$$\theta_C(s) = \theta_E(s) + \theta_F(s) \tag{55}$$

$$\theta_E(s) = \frac{s + K_C}{K_A K_C}\,\delta(s) \tag{56}$$

$$\theta_F(s) = (K_R s + 1)\left[\theta(s) - \sigma_1(RG)\,q_1(s) - \sigma_2(RG)\,q_2(s)\right] . \tag{57}$$

Substituting Equations 56 and 57 into Equation 55 yields

$$\begin{aligned}\theta_C(s) = {} & \left[K_R s + 1\right]\theta(s) - \sigma_1(RG)\left[K_R s + 1\right] q_1(s) \\ & - \sigma_2(RG)\left[K_R s + 1\right] q_2(s) + \frac{s + K_C}{K_A K_C}\,\delta(s) .\end{aligned} \tag{58}$$

Equation 58 is the control law, and it can be combined with the forward-loop system of Equation 38 to yield Equation 59.

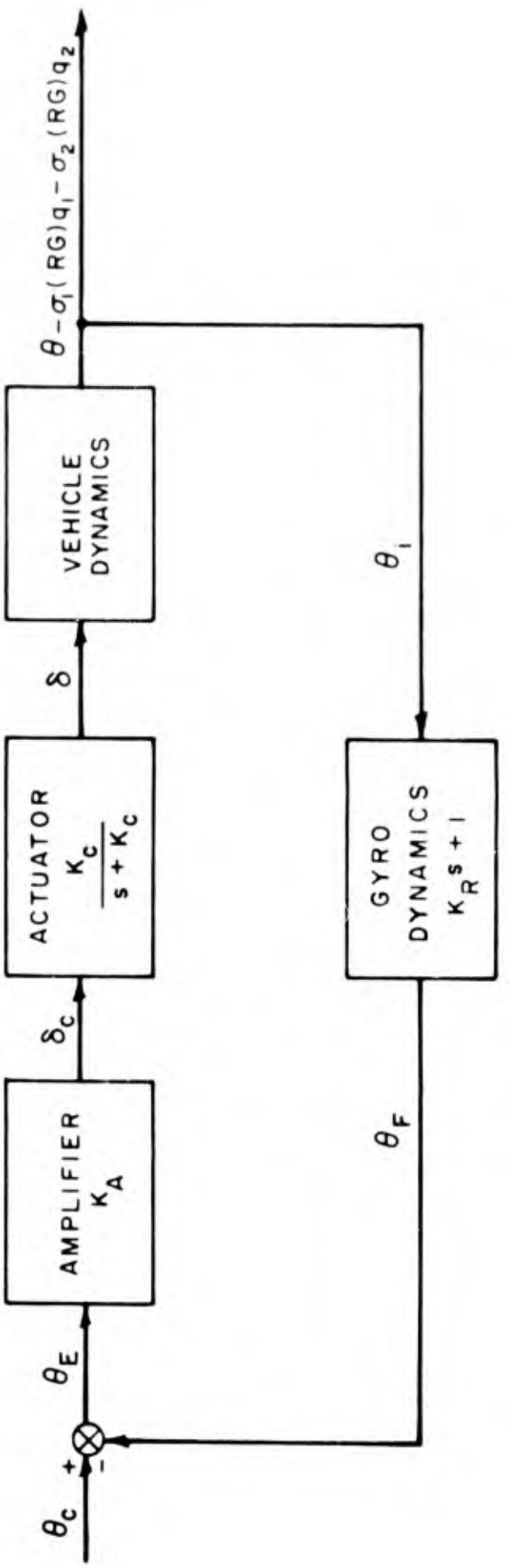

Figure 6. System Block Diagram

$$\begin{bmatrix} (1860s+51.6) & -1859s & (-.0647s-4.682)(.01933s-7.66) & -81.0 \\ .1143 & (s^2+.0755s)(.001326s-.087)(-.000815s-.0097) & & -1.042 \\ -29.3 & 3.27s & (s^2+.1285s+.312)(-.0482s+5.107) & 19.72 \\ 8.55 & -1.96s & (-.05175s+2.013)(s^2+.087s+8.181) & 19.25 \\ 0 & (K_R s+1) & -\sigma_1(RG)(K_R s+1) \quad -\sigma_2(RG)(K_R s+1) & \frac{s+K_C}{K_A K_C} \end{bmatrix} \begin{Bmatrix} \alpha(s) \\ \theta(s) \\ q_1(s) \\ q_2(s) \\ \delta(s) \end{Bmatrix} =$$

$$\begin{Bmatrix} 0 \\ 0 \\ 0 \\ 0 \\ 1 \end{Bmatrix} \theta_c(s) + \begin{Bmatrix} -51.6 \\ -.1143 \\ 29.3 \\ -8.55 \\ 0 \end{Bmatrix} \alpha_g(s) \qquad (59)$$

The determinant of the square matrix of coefficients in matrix Equation 59 is the closed-loop characteristic stability determinant. The characteristic equation is obtained by expanding this determinant and setting the resulting polynomial equal to zero.

Recalling that the uncoupled short-period characteristics of the forward-loop were $\omega_{sp} = .342$ rad/sec and $\zeta_{sp} = .151$, assume that it is desired to augment this through the control loop to values of $\omega_{sp} = 2$ rad/sec and $\zeta_{sp} = .5$. Neglecting elasticity and considering at first only the rigid-body motion, the stability determinant becomes

$$\begin{vmatrix} (1860s+51.6) & -1859s & -81.0 \\ .1143 & (s^2+.0755s) & -1.042 \\ 0 & (K_R s+1) & \left(\frac{1}{K_A K_C}s + \frac{1}{K_A}\right) \end{vmatrix} = 0. \qquad (60)$$

Expanding the determinant, the characteristic equation becomes

$$s^4 + \left[K_c + .1032 \right] s^3 + \left[.1032 K_c + 1940 K_A K_c K_R + .1164 \right] s^2$$

$$+ \left[.1164 K_c + 44.53 K_A K_c K_R + 1940 K_A K_c \right] s + 44.53 K_A K_c = 0. \qquad (61)$$

It is known that Equation 61 will have the form

$$(s + a)(s + b)(s^2 + 2\zeta_{sp}\omega_{sp} s + \omega_{sp}^2) = 0. \qquad (62)$$

Expanding Equation 62 one has

$$s^4 + \left[2\zeta_{sp}\omega_{sp} + (a + b) \right] s^3 + \left[\omega_{sp}^2 + ab + 2\zeta_{sp}\omega_{sp}(a + b) \right] s^2$$

$$+ \left[\omega_{sp}^2 (a + b) + 2\zeta_{sp}\omega_{sp} ab \right] s + \omega_{sp}^2 ab = 0. \qquad (63)$$

Matching coefficients in Equations 61 and 63 gives

$$K_c + .1032 = 2\zeta_{sp}\omega_{sp} + (a + b) \qquad (64)$$

$$.1032 K_c + 1940 K_A K_c K_R + .1164 = \omega_{sp}^2 + ab + 2\zeta_{sp}\omega_{sp}(a + b) \qquad (65)$$

$$.1164 K_c + 44.53 K_A K_c K_R + 1940 K_A K_c = \omega_{sp}^2 (a + b) + 2\zeta_{sp}\omega_{sp} ab \qquad (66)$$

$$44.53 K_A K_c = \omega_{sp}^2 ab. \qquad (67)$$

Substituting ω_{sp} = 2 rad/sec and ζ_{sp} = .5 into the above four equations gives

$$K_c - (a + b) = 1.897 \tag{68}$$

$$.1032 K_c + 1940 K_A K_c K_R - 2(a + b) - ab = 3.884 \tag{69}$$

$$.1164 K_c + 44.53 K_A K_c K_R + 1940 K_A K_c - 2ab - 4(a + b) = 0 \tag{70}$$

$$44.53 K_A K_c - 4ab = 0. \tag{71}$$

There are four equations and five unknowns. The system of equations can be solved if a value is assumed for one of the unknowns. Assume K_C = 10, which is a typical value for actuator gain; K_C is taken as constant since K_A and K_R are more easily varied in the physical control system. This yields

$$a + b = 8.103 \tag{72}$$

$$2(a + b) + ab + 2.852 = 19,400 K_A K_R \tag{73}$$

$$4(a + b) + 2ab - 1.164 = 19,400 K_A + 445.3 K_A K_R \tag{74}$$

$$4ab = 445.3 K_A . \tag{75}$$

Solving these last four equations yields

$$K_A = .0016; \quad K_R = .618; \quad a = 8.077; \quad b = .027.$$

These are the gain values which will give the desired short-period characteristics when elasticity is not considered. The two real roots s = -8.077 and s =-.027 yield the decay time constants for the actuator and gyro transient behavior.

To demonstrate the severity of the mode interaction phenomenon in the closed-loop case, the first elastic mode will be added to the system. To do this, a location must be picked for the rate and attitude gyro package since the value of the mode shape slope σ_1(RG) is needed at the sensor location. The closed-loop transient dynamics are normally

somewhat sensitive to sensor location; but for the time being, arbitrarily select station 60. At this location, $\sigma_1(RG) = .0638$. Using the gains determined above, the stability determinant becomes

$$\begin{vmatrix} (1860s + 51.6) & -1859s & (-.0647s - 4.682) & -81.0 \\ .1143 & (s^2 + .0755s) & (.001326s - .087) & -1.042 \\ -29.3 & 3.27s & (s^2 + .1285s + .312) & 19.72 \\ 0 & (.618s + 1) & (-.0395s - .0638) & (62.5s + 625) \end{vmatrix} = 0. \quad (76)$$

Expansion of Equation 76 and factorization of the resulting sixth-order polynomial gives the following form:

$$(s - 1.08)(s + 1.28)(s^2 + .0406s + 1.817)(s + 10)s = 0. \quad (77)$$

Here it is seen that the interaction has resulted in real short-period roots inditical with those of the open-loop case (Equation 40). Also, the elastic mode quadratic is nearly the same as in the open-loop case. This result says that although these rigid-body-established gain values give the desired short-period response when only the rigid-body motion is considered, when the elastic mode is added the coupled short-period and elastic mode transient dynamics are almost totally insensitive to the control system, reverting back to their open-loop behavior. The significance of this result is that the conventional synthesis procedure of using a rigid-body-only analysis to arrive at "ball park" estimates for various control element gains can no longer be used when strong mode interaction exists. The "first cut" in preliminary design of a control system for this type of vehicle must include the significant elastic modes.

When the second elastic mode is also included, the characteristic equation obtained by using the same gain values as used above is

$$(s - 1.31)(s + 1.54)(s^2 + .025s + 1.328)(s^2 + .0603s + 9.3)(s + 10)s = 0. \quad (78)$$

This again is nearly identical transient behavior with the open-loop case (Equation 41).

To see what effect sensor location has on the closed-loop dynamics, assume the gyro package is at station 400. This location gives mode slope values of $\sigma_1(RG) = \sigma_2(RG) = -.032$ (see Figure 5). Again using the same gains, one obtains the polynomials given in Equation 79 including one elastic mode and Equation 80 including two elastic modes.

$$(s-1.08)(s+1.28)(s^2+.039s+1.181)(s+10)s = 0 \tag{79}$$

$$(s-1.31)(s+1.54)(s^2+.024s+1.32)(s^2+.061s+9\ 3)(s+10)s = 0. \tag{80}$$

Placing the gyro package at station 304, where $\sigma_1(RG) = \sigma_2(RG) = 0$, gives the following characteristic equations, including first one then two elastic modes:

$$(s-1.08)(s+1.28)(s^2+.040s+1.81)(s+10)s = 0 \tag{81}$$

$$(s-1.31)(s+1.54)(s^2+.026s+1.33)(s^2+.061s+9.3)(s+10)s = 0. \tag{82}$$

Comparison of Equations 77, 79, 81 and Equations 78, 80, 82 shows that sensor location has almost no effect on the transient dynamics in the presence of strong mode interaction. However, it should be kept in mind that sensor location is important and has very pronounced effects on transient dynamics when the modal frequencies are sufficiently separated to eliminate the interaction phenomenon. In the examples presented here, the interaction is so strong that it completely dominates the additional terms introduced by the feedback control system.

The strong interaction between rigid-body and elastic motion creates the unfortunate position of not being able to achieve the desired closed-loop- short-period characteristics using a conventional approach to design. There is also the disturbing thought that quite possibly no combination of gains K_A, K_C, and K_R exists which will give the desired behavior of $\omega_{sp} = 2$ rad/sec and $\zeta_{sp} = .5$. If this proves true, then something more sophisticated than rate-attitude feedback must be used (here there is a hint of things to come - namely, active control of the elastic modes).

With the gyro package at station 60, the stability determinant of Equation 59 can be expanded to give

$$s^8 + \left[.319 + K_C\right]s^7 + \left[8.63 + .319K_C + .114K_AK_CK_R\right]s^6 + \left[2.61 + 8.63K_C + .114K_AK_C + .261K_AK_CK_R\right]s^5 + \left[-9.1 + 2.61K_C + .261K_AK_C + 11.75K_AK_CK_R\right]s^4 + \left[2.27 - 9.1K_C + 11.75K_AK_C + 3.74K_AK_CK_R\right]s^3 + \left[-24.9 + 2.27K_C + 3.74K_AK_C - 30.7K_AK_CK_R\right]s^2 + \left[-24.9K_C - 30.7K_AK_C - .001435K_AK_CK_R\right]s + \left[-.001435K_AK_C\right] = 0. \tag{83}$$

This is the characteristic equation in terms of control element gains. One would like the characteristic equation to be of the form

$$(s+a)(s+b)(s^2+2\zeta_{sp_c}\omega_{sp_c}s+\omega_{sp_c}^2)(s^2+2\zeta_{1e}\omega_{1e}s+\omega_{1e}^2)(s^2+2\zeta_{2e}\omega_{2e}s+\omega_{2e}^2)=0 \quad (84)$$

Expanding Equation 84 and equating coefficients to those of Equation 83 yields eight equations with eleven unknowns. Clearly, to solve these simultaneously three of the unknown parameters must be known or specified. As before, it is specified that $K_c = 10$; also wanted is ω_{sp} and ζ_{sp} to be 2 rad/sec and .5, respectively. This reduces the system to eight equations with eight unknowns, which has a unique solution. Omitting the details of the solution, the unknown gains must be $K_A = 1.8$ and $K_R = .618$. Unfortunately, the above procedure will not in general yield the desired short-period response since there is no way of ensuring that the specified frequency and damping ratio will correspond to the short-period mode rather than one of the elastic modes. Indeed, as will be seen later, it is the first coupled elastic mode which takes on the specified frequency and damping ratio when the above gains are used, rather than the short-period mode.

To help determine if there is any combination of gains K_A, K_c, and K_R which will give the desired short-period dynamics, a series of root locus plots will be made where these gains are varied in a systematic manner. The system block diagram of Figure 6 can be rearranged into an equivalent form given in Figure 7. The total pitch angle θ_i as seen by the sensor is composed of rigid-body and elastic mode components and is given by

$$\theta_i = \theta - \sigma_1(RG)q_1 - \sigma_2(RG)q_2 \quad . \quad (85)$$

Dividing by $\delta_1(s)$ gives the form

$$\frac{\theta_i}{\delta_1} = \frac{\theta}{\delta_1} - \sigma_1(RG)\frac{q_1}{\delta_1} - \sigma_2(RG)\frac{q_2}{\delta_1} \quad (86)$$

or

$$\frac{\theta_i}{\delta_1} = \left[\left(\frac{\theta}{\delta}\right) - \sigma_1(RG)\left(\frac{q_1}{\delta}\right) - \sigma_2(RG)\left(\frac{q_2}{\delta}\right)\right]\frac{\delta}{\delta_1} \quad . \quad (87)$$

The terms in parentheses in Equation 87 are forward-loop transfer functions and can be put in the form

$$\frac{\theta(s)}{\delta(s)} = A_\theta\frac{N_\theta}{\Delta} \; ; \quad \frac{q_1(s)}{\delta(s)} = A_{q_1}\frac{N_{q_1}}{\Delta} \; ; \quad \frac{q_2(s)}{\delta(s)} = A_{q_2}\frac{N_{q_2}}{\Delta}$$

where A_θ, A_{q_1}, and A_{q_2} are numerical gains; and N_θ, N_{q_1}, N_{q_2}, and Δ are normalized polynomials in the Laplace variable s. It is also seen from Figure 7 that

$$\frac{\delta(s)}{\delta_i(s)} = -\frac{K_A K_C K_R (s + \frac{1}{K_R})}{s + K_C} \quad . \tag{88}$$

Equation 87 therefore becomes

$$\frac{\theta_i}{\delta_i} = \frac{K_A K_C K_R (s + \frac{1}{K_R}) \left[A_\theta N_\theta - \sigma_1 (RG) A_{q_1} N_{q_1} - \sigma_2 (RG) A_{q_2} N_{q_2} \right]}{(s + K_C)\,\Delta} \tag{89}$$

Referring to Figure 7 it is seen that the closed-loop transfer function is

$$\frac{\theta_i}{\theta_c} = \left[\frac{\frac{\theta_i}{\delta_i}}{1 + \frac{\theta_i}{\delta_i}} \right] \frac{\frac{1}{K_R}}{s + \frac{1}{K_R}} \quad . \tag{90}$$

Disregarding the gyro lag term, the system characteristic equation is

$$\frac{\theta_i}{\delta_i} + 1 = 0 \, . \tag{91}$$

θ_1/δ_1 given in Equation 89 is the open-loop transfer function. The three forward-loop transfer functions mentioned above can be obtained by applying Cramer's rule to matrix Equation 38. When the determinants are expanded, a ratio of polynomials results for each transfer function. These polynomials are then factored to give the forms in Equations 92, 93, and 94 below.

$$\frac{\theta(s)}{\delta(s)} = \frac{1.04(s-1.148)(s+.00011)(s+1.343)(s+.027 \pm j\,2.865)}{s(s-1.31)(s+1.543)(s+.012 \pm j\,1.15)(s+.031 \pm j\,3.051)} \tag{92}$$

$$\frac{q_1(s)}{\delta(s)} = \frac{-19.72(s-1.562)(s+1.912)(s-.00235 \pm j\,2.183)s}{\Delta} \tag{93}$$

$$\frac{q_2(s)}{\delta(s)} = \frac{-19.25(s-1.062)(s+1.229)(s+.0156 \pm j\,.365)s}{\Delta} \tag{94}$$

where Δ is the same denominator for all three equations. These three transfer functions can be incorporated into Equation 89 along with the $\sigma_1(RG)$ and $\sigma_2(RG)$ values for the sensor package location at station 60 to give, after further factorization,

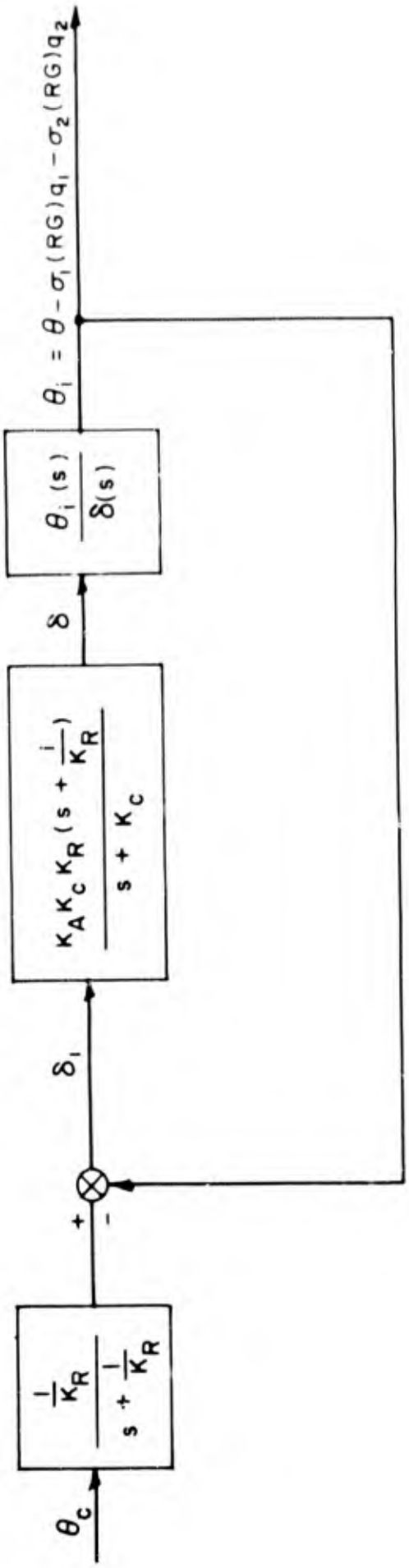

Figure 7. Equivalent System

$$\frac{\theta_i}{\delta_i} = \frac{.113 K_A K_C K_R \left(s + \frac{1}{K_R}\right)(s + .0000467)(s - 1.44)(s + 1.8)(s + .975 \pm j10.25}{s(s + K_C)(s - 1.31)(s + 1.543)(s + .012 \pm j1.15)(s + .031 \pm j3.051)} \quad (95)$$

Equation 95 is in a form suitable for root locus plots.

By assuming various values for K_C and K_R, the loci can be plotted as a function of gain K_A. With the use of an IBM 7094 digital computer program, twenty root loci were generated in which all significant combinations of the relative locations of the $(s + K_C)$ and $(s + 1/K_R)$ pole-zero factors were investigated. None of these combinations allowed the realization of the desired closed-loop short-period dynamics. Root locus plots for three of the combinations of K_C and K_R which gave the most widely differing characteristics are shown in Figures 8, 9, and 10. (Only the two upper quadrants are shown.)

It is seen in Figure 8 that for $K_C = 10$ and $K_R = 0.618$, the short-period mode remains separated into two real roots, one positive and one negative, for all values of K_A. For $K_A = 1.8$ the coupled first elastic mode has an undamped frequency and damping ratio of $\omega_{1e} = 2$ rad/sec and $\zeta_{1e} = 0.5$, respe tively, which confirms that the analysis of Equations 83 and 84 (see pages 33 and 34) with these same gain values, will not give the desired short-period results. Figure 8 also shows that the two real roots corresponding to the short-period mode are extremely insensitive to K_A throughout its entire range, zero to infinity. Another interesting and unconventional result is that for large K_A the frequency of the first elastic mode is higher than that of the second elastic mode. In fact, as $K_A \to \infty, \omega_{1e} \to \infty$, while $\omega_{2e} \to 10.3$.

In Figure 9 ($K_C = 10$; $K_R = -.33$) the two elastic modes have loci similar to those in Figure 8. However, there is a range of gains for K_A where an oscillatory, albeit unstable, mode exists.

Figure 10 shows a range of K_A where there is a stable oscillatory "pseudo" short-period mode. However, it does not come close to the desired point of $\omega_{sp_c} = 2$ rad/sec and $\zeta_{sp_c} = .5$. This oscillatory mode emanates from the branch formed between a short-period pole and the actuator pole and is thus not a true short-period motion as it would be if it came from a branch due entirely to short-period poles. In terms of time histories of transient motion, it is of little consequence whether the frequencies and damping are true or "pseudo" short-period in origin; the histories are a function of the closed-loop roots, regardless of their origin from open-loop poles. Other loci plots using moderate variations in K_C and K_R about those values used in Figure 10 show no improvement in short-period characteristics over those of Figure 10. Notice also that it is now the first elastic mode which is unstable while the second is stable. The frequencies ω_{1e} and ω_{2e} still exhibit the same trends with increasing K_A as in Figures 8 and 9.

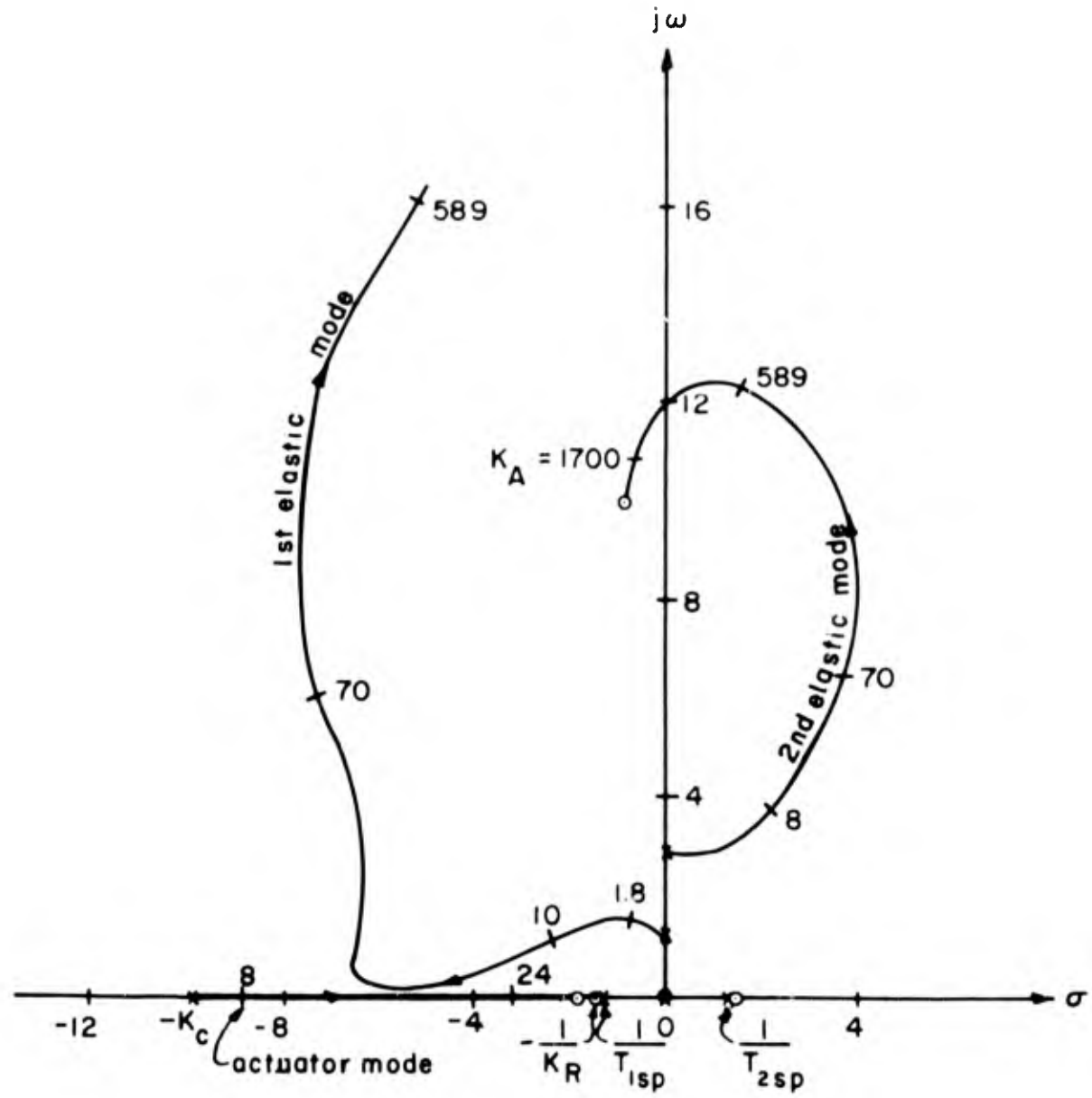

Figure 8. Root Locus of θ_i / δ_1
(K_c = 10; K_R = .618)

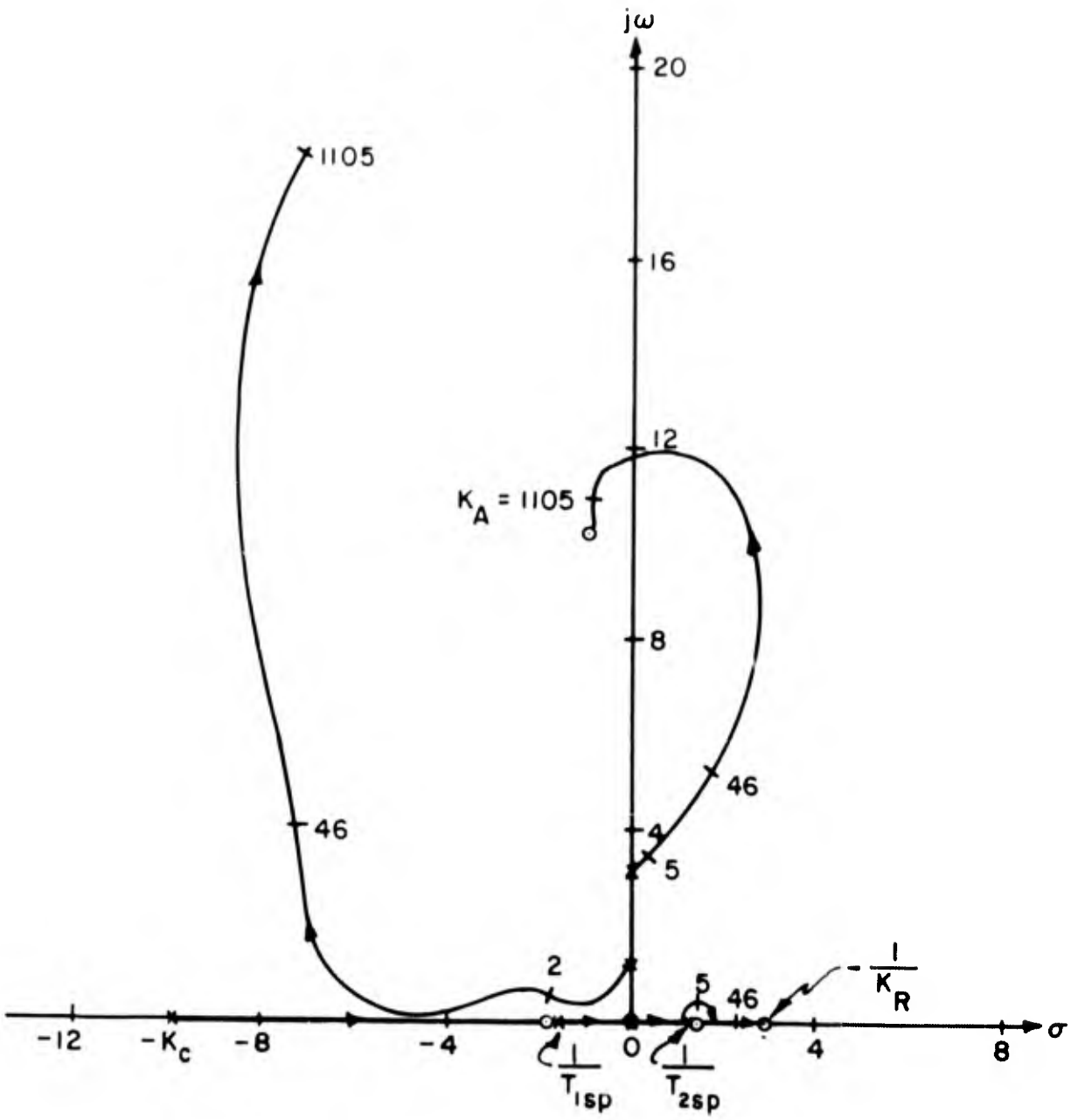

Figure 9. Root Locus of θ_i / δ_i
(K_c = 10; K_R = -.33)

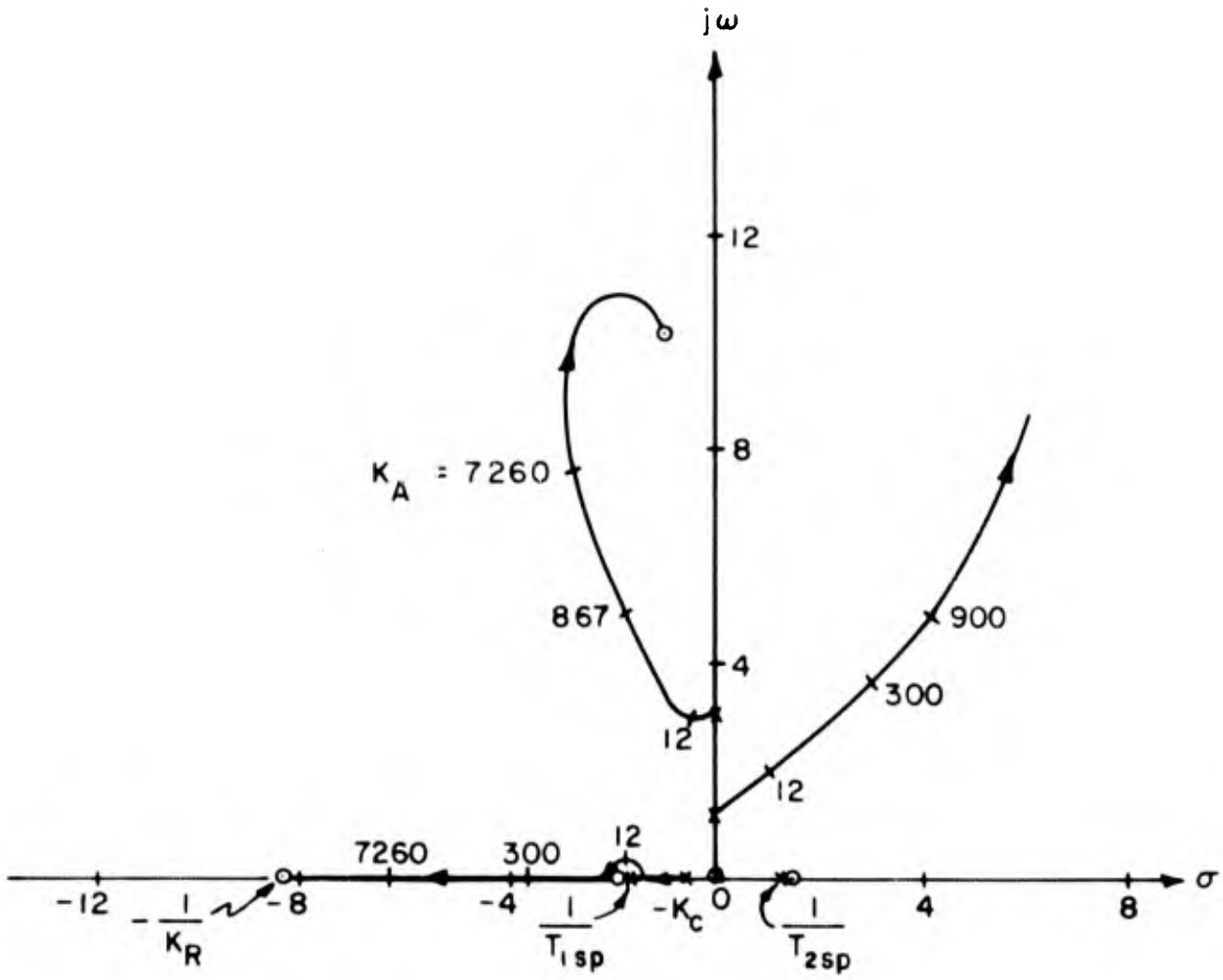

Figure 10. Root Locus of θ_i / δ_1
($K_c = .5$; $K_R = .12$)

It is evident from the many root locus plots generated for the open-loop transfer function in Equation 95 that there is no combination of gains K_A, K_c, and K_R which will give the desired closed-loop short-period characteristics. There is, however, one other facet of this system which should be looked at briefly. Assume, for the moment, that only the rigid-body component of the pitch signal θ_1 is fed back to the controller. This assumes that the elastic components can be separated from the rigid-body component by some suitable technique such as the McDonnell digital adaptive filter, the Minneapolis-Honeywell gyro blending technique, or possibly even conventional filtering if the coupled frequencies are sufficiently separated. The open-loop transfer function as given by Equation 89 would then be

$$\frac{\theta_1}{\delta_1} = \frac{\theta}{\delta_1} = \frac{1.04 K_A K_c K_R \left(s + \frac{1}{K_R}\right)(s - 1.148)(s + .00011)(s + 1.343)(s + .027 \pm j\,2.865)}{s(s + K_c)(s - 1.31)(s + 1.543)(s + .012 \pm j\,1.15)(s + .031 \pm j\,3.051)} \cdot \quad (96)$$

After sone "cut-and try" iterations, a combination of values for K_c and K_R was found which gave a root locus plot of Equation 96 that would yield approximately the desired closed-loop short-period dynamics. This is shown in Figure 11. Gains of $K_c = 1.75$, $K_R = -.286$, and $K_A = -3.14$ will provide $\omega_{sp_c} = 2.04$ rad/sec and $\zeta_{sp_c} = .591$. But the surprising result here is that for this K_A value the first elastic mode is overdamped, resulting in two negative real roots, -.00027 and -1.291. The system is unstable, however, due to the two positive real roots, 1.375 and .42. The coupled second elastic mode is only slightly changed from its uncoupled characteristics; it has $\omega_{2e} = 3.05$ rad/sec and $\zeta_{2e} = .026$. It is evident in this case that the second elastic mode has only a very slight effect on the interaction phenomenon. It appears that were it not for the two positive real roots, this would be a suitable control system as far as providing the desired short-period dynamics is concerned. It provides no artificial stiffening of the structure, however. In addition, the implementation of either of the two sophisticated filtering techniques mentioned above is quite complex.

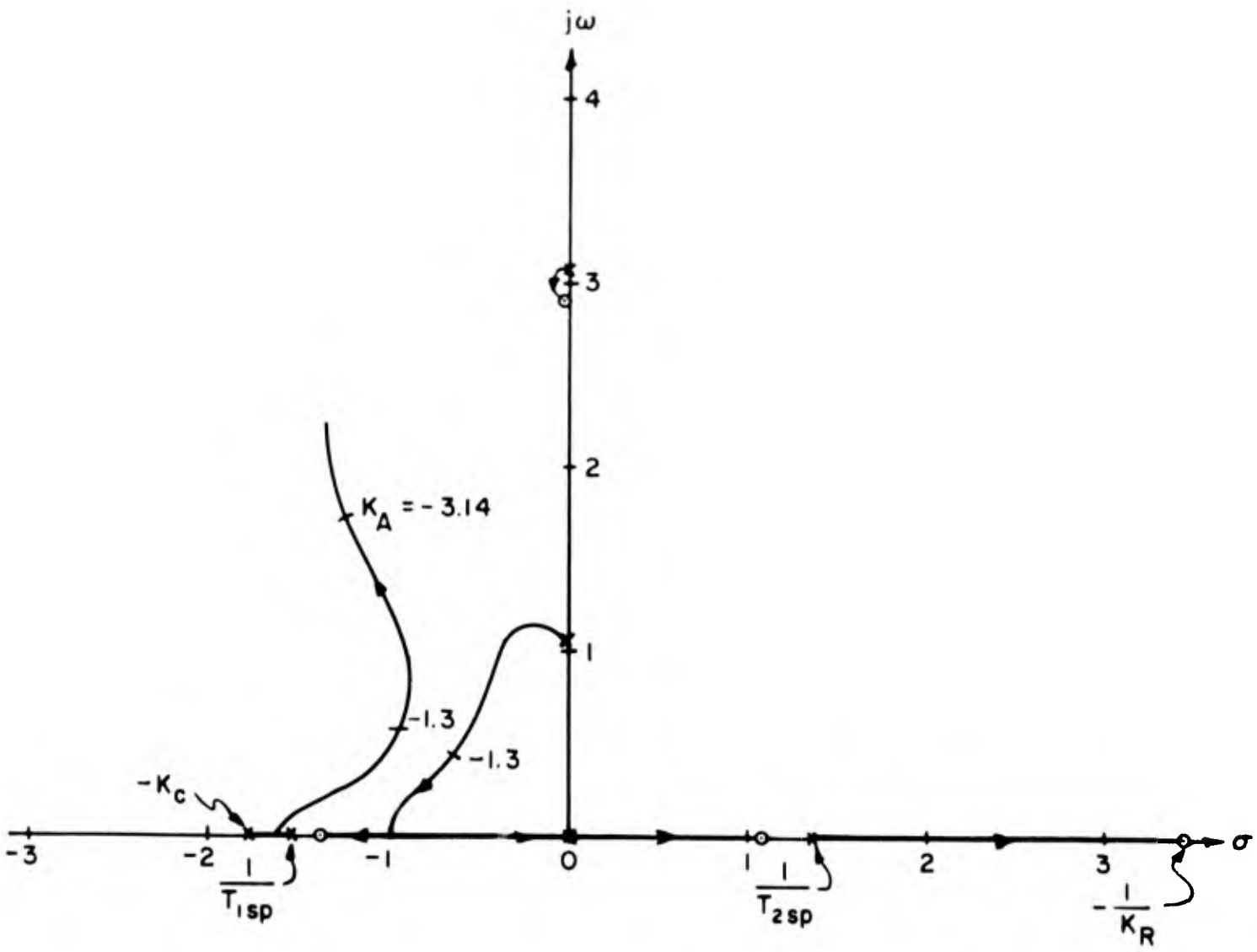

Figure 11. Root Locus of θ/δ_1
(K_c = 1.75; K_R = -.286; no elastic feedback)

SECTION V

CLOSED-LOOP TRANSIENT DYNAMICS UNDER ACTIVE CONTROL - SINGLE INNER-LOOP SENSOR

The previous four sections have provided the necessary preliminary data and background information for understanding the nature of the mode interaction problem for this vehicle. It has been shown that the coupling phenomena can cause a rigid-body static divergence for an aerodynamically statically stable rigid configuration in the uncontrolled or forward-loop-only case. In the closed-loop case the coupling prevents the use of a rigid-body-only analysis to arrive at preliminary values for the various control element gains. In fact, even with the elastic modes included, desired closed-loop short-period behavior cannot generally be achieved with a pitch rate and attitude feedback control unless the elastic components are filtered or otherwise removed from the feedback signal.

This brings up the main topic of this dissertation, namely, active control of the elastic modes as well as the rigid-body motion. There is the theory that if the closed-loop, coupled elastic mode frequencies can be increased sufficiently by appropriate control inputs, then there should result a lessening of the interaction between rigid-body and elastic motion and possibly a simpler overall control system in terms of required component sophistication. Also, other benefits may be possible such as use of a lighter structure due to the added artificial stiffness.

As a first attempt at actively controlling the elastic modes, consider what can be done using linear rate and displacement sensing and feedback to the main engine thrust vector. In an inertial coordinate system, the linear normal displacement at a point on the vehicle's elastic axis is given by

$$z = z_{CG} + (\ell_z - \ell_{CG})\theta - \phi_1(z)q_1 - \phi_2(z)q_2 \quad . \tag{97}$$

Note that this z is a deflection in an inertial system and is not the z of the stability axes system.

Consider the block diagram of Figure 12. The signal coming from the (z/δ) transfer function is passed through an ideal linear rate and displacement sensor and then through an ideal high-pass filter to block the rigid-body components of the signal, which will be of lower frequency than the elastic mode components once the total system is successfully synthesized. The total pitch attitude signal θ_1 as sensed by the ideal angular rate and attitude gyro is sent through an ideal low-pass filter to yield only the rigid-body component of the pitch signal which is subtracted from the programmed input θ_c to give an error signal. All components are considered ideal purely for analysis convenience. This restriction would, of course, be removed once the basic control system had been synthesized. Hopefully, as has generally been true in the past, a scheme workable in the idealized case would also work, with reasonable modifications, in a more practical case.

The diagram of Figure 12 can be put in the equivalent forms shown in Figures 13 and 14,

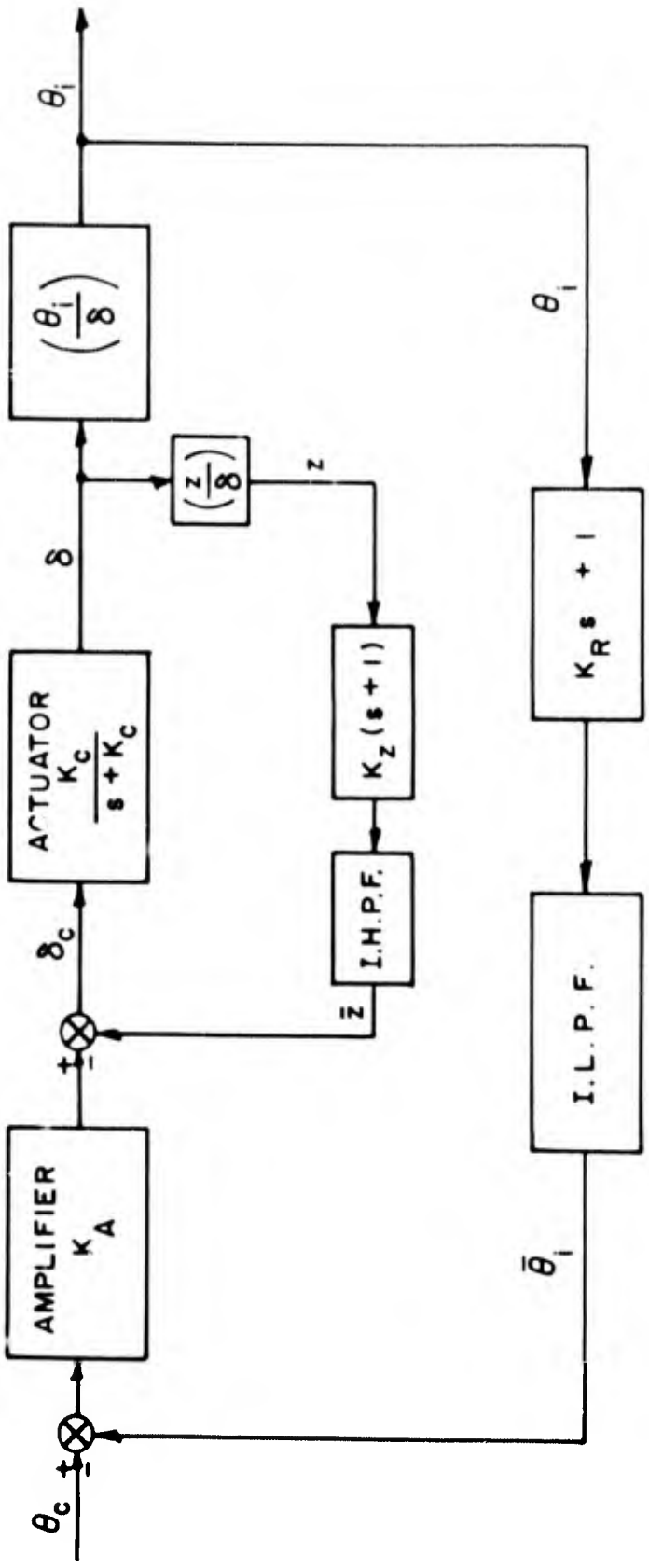

Figure 12. System Block Diagram

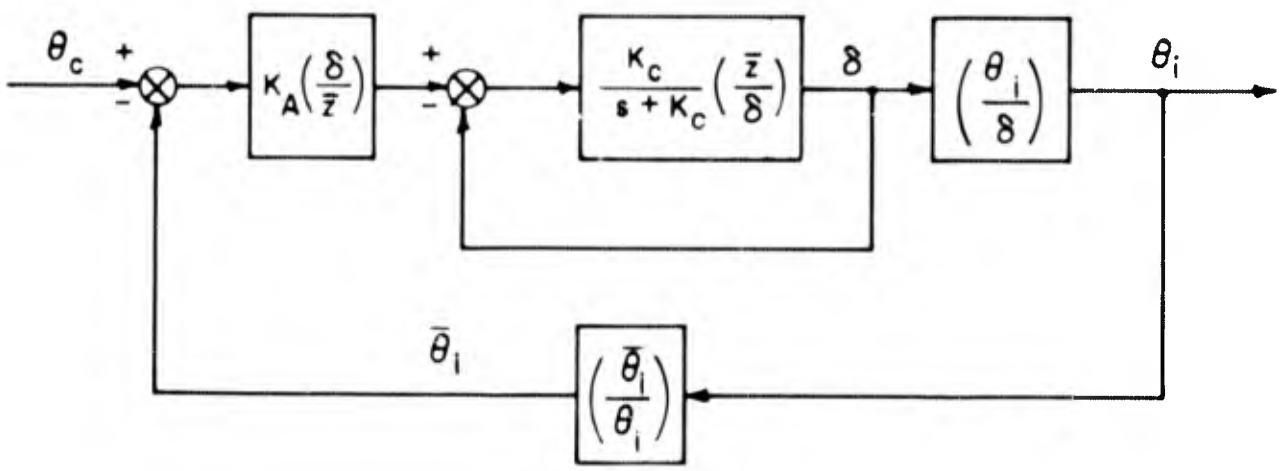

Figure 13. Equival ent System

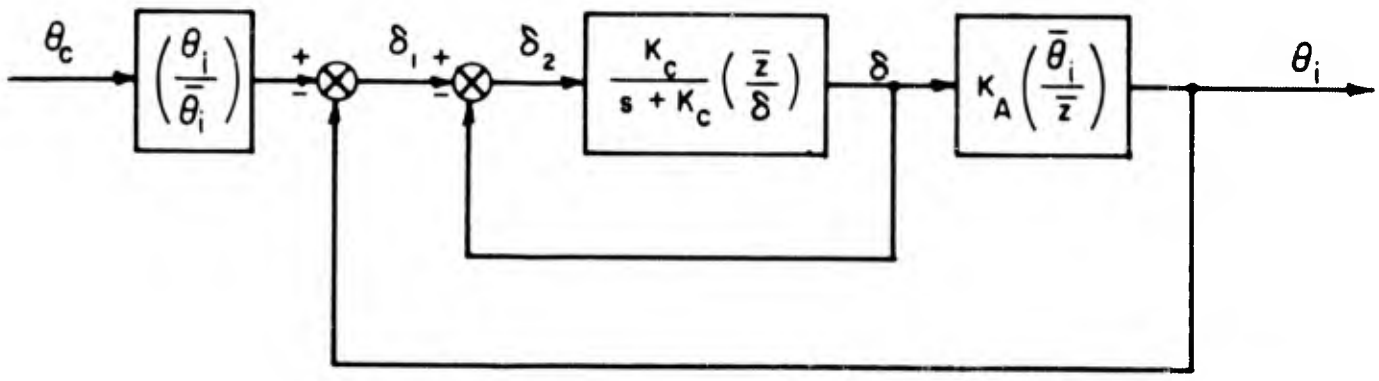

Figure 14. Equival ent System

where

$$\bar{\theta}_i = (K_R s + 1)\theta \tag{98}$$

$$\bar{z} = -K_z(s+1)\left[\phi_1(z)q_1 + \phi_2(z)q_2\right] \tag{99}$$

$$\left(\frac{\bar{z}}{\delta}\right) = -K_z(s+1)\left[\phi_1(z)\left(\frac{q_1}{\delta}\right) + \phi_2(z)\left(\frac{q_2}{\delta}\right)\right] \tag{100}$$

$$\left(\frac{\bar{\theta}_i}{\delta}\right) = K_R\left(s + \frac{1}{K_R}\right)\left(\frac{\theta}{\delta}\right) \tag{101}$$

$$\left(\frac{\bar{\theta}_i}{\theta_i}\right) = \frac{K_R\left(s + \frac{1}{K_R}\right)\left(\frac{\theta}{\delta}\right)}{\left(\frac{\theta}{\delta}\right) - \sigma_1(RG)\left(\frac{q_1}{\delta}\right) - \sigma_2(RG)\left(\frac{q_2}{\delta}\right)} \tag{102}$$

$$\frac{K_c}{s+K_c}\left(\frac{\bar{z}}{\delta}\right) = \frac{-K_c K_z(s+1)\left[\phi_1(z)\left(\frac{q_1}{\delta}\right) + \phi_2(z)\left(\frac{q_2}{\delta}\right)\right]}{s + K_c} \tag{103}$$

$$K_A\left(\frac{\bar{\theta}_i}{\bar{z}}\right) = \frac{K_A K_R\left(s + \frac{1}{K_R}\right)\left(\frac{\theta}{\delta}\right)}{-K_z(s+1)\left[\phi_1(z)\left(\frac{q_1}{\delta}\right) + \phi_2(z)\left(\frac{q_2}{\delta}\right)\right]}\,. \tag{104}$$

Using notation introduced in Section IV, Equations 102, 103, and 104 can be put in the following form:

$$\left(\frac{\bar{\theta}_i}{\theta_i}\right) = \frac{K_R A_\theta\left(s + \frac{1}{K_R}\right)N_\theta}{A_\theta N_\theta - \sigma_1(RG)A_{q_1}N_{q_1} - \sigma_2(RG)A_{q_2}N_{q_2}} \tag{105}$$

$$\frac{K_c}{s+K_c}\left(\frac{\bar{z}}{\delta}\right) = \frac{-K_c K_z(s+1)\left[\phi_1(z)A_{q_1}N_{q_1} + \phi_2(z)A_{q_2}N_{q_2}\right]}{(s+K_c)\Delta} \tag{106}$$

$$K_A\left(\frac{\bar{\theta}_i}{\bar{z}}\right) = \frac{K_A K_R A_\theta\left(s + \frac{1}{K_R}\right)N_\theta}{-K_z(s+1)\left[\phi_1(z)A_{q_1}N_{q_1} + \phi_2(z)A_{q_2}N_{q_2}\right]} \tag{107}$$

Once a sensor location is chosen and also a value for K_c, a root locus plot of the open-inner-loop transfer function of Equation 106 can be made as a function of sensor gain K_z. Plots were made for several sensor locations, stations 20, 140, 300, and 420, but the one which resulted in the best system is discussed below. This location is body station 140. It is seen in Figure 5 that this is the first anti-node of the second elastic mode. For this location, and the same configuration as previously used, Equations 106 and 107 have the following numerical forms:

$$\frac{K_c}{s+K_c}\left(\frac{\bar{z}}{\delta}\right) = \frac{135.6\,K_cK_z(s+1)(s-3.2\pm j\,2.625)(s+3.315\pm j\,3.81)s}{(s+K_c)(s-1.31)(s+1.543)(s+.012\pm j1.15)(s+.031\pm j3.051)s} \tag{108}$$

$$K_A\left(\frac{\bar{\theta}_i}{\bar{z}}\right) = \frac{1.04\,K_AK_R\left(s+\frac{1}{K_R}\right)(s-1.148)(s+.00011)(s+1.343)(s+.027\pm j2.865)}{135.6\,K_z(s+1)(s-3.2\pm j\,2.625)(s+3.315\pm j\,3.81)s} \tag{109}$$

The open-loop transfer function for the outer-loop in Figure 14 is

$$\left(\frac{\theta_i}{\delta_1}\right) = \frac{\frac{K_AK_c}{s+K_c}\left(\frac{\bar{\theta}_i}{\delta}\right)}{1+\frac{K_c}{s+K_c}\left(\frac{\bar{z}}{\delta}\right)} \tag{110}$$

or, from Equations 108 and 109,

$$\left(\frac{\theta_i}{\delta_1}\right) = \frac{1.04K_AK_cK_R\left(s+\frac{1}{K_R}\right)(s-1.148)(s+.00011)(s+1.343)(s+.027\pm j2.865)}{\left[\text{Closed — loop roots of inner-loop}\right]} \tag{111}$$

Notice that there is somewhat of an iteration process required between the root loci of Equations 108 and 111 in order to arrive at satisfactory dynamics. That is, the poles of 111 depend on the closed-loop roots of 108. The root locus of Equation 108 is shown in Figure 15 as a function of K_z for $K_c = 10$. The locus for the first elastic mode is mostly in the right-half plane, indicating an unstable condition. The frequency of the second mode increases towards infinity with increasing K_z. However, the first mode frequency is not increased much with increasing gain. It is evident that a single sensor feedback on the inner-loop does not provide the desired increase in both elastic mode frequencies with increasing K_z. The short-period (again, "pseudo" short-period) locus does appear good in Figure 15, however, and the outer-loop will be closed using Equation 111 to see the total system behavior. For closed-loop roots of the inner-loop at $K_z = .054$ (see Figure 15) and for $K_r = .05$, the root locus of Equation 111 is shown in Figure 16 as a function of K_A. At a gain $K_A = 39$ one has the desired closed-loop short-period dynamics, $\omega_{sp_c} = 2$ rad/sec, $\zeta_{sp_c} = .5$. However, the first elastic mode now has a lower frequency than the short-period mode which, of course, is unacceptable since the outer-loop is being low-pass filtered. All other relative combinations of K_c, K_z, and K_R gave worse characteristics than the system represented by the loci of Figures 15 and 16. This was verified by considering all relative locations for the pole and zero factors containing K_c and K_R.

It has been shown that a single inner-loop sensor providing linear rate and displacement feedback does not provide the desired stiffening for both elastic modes. Possibly the job can be done with two suitably placed sensors. This will be studied in the next section.

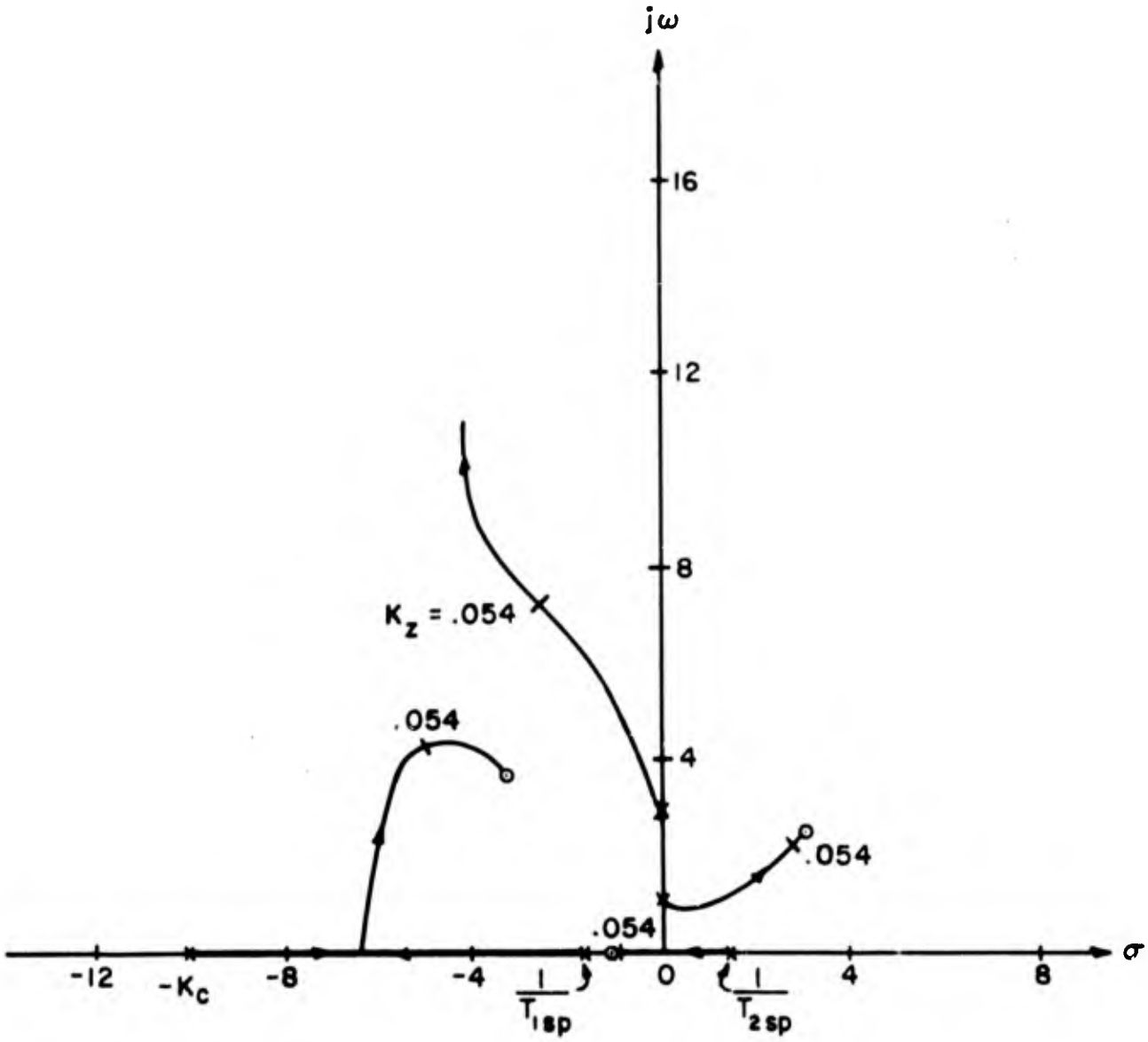

Figure 15. Root Locus of $\frac{K_c}{s + K_c}\left(\frac{\overline{Z}}{\delta}\right)$
(K_c = 10; sensor at sta 140)

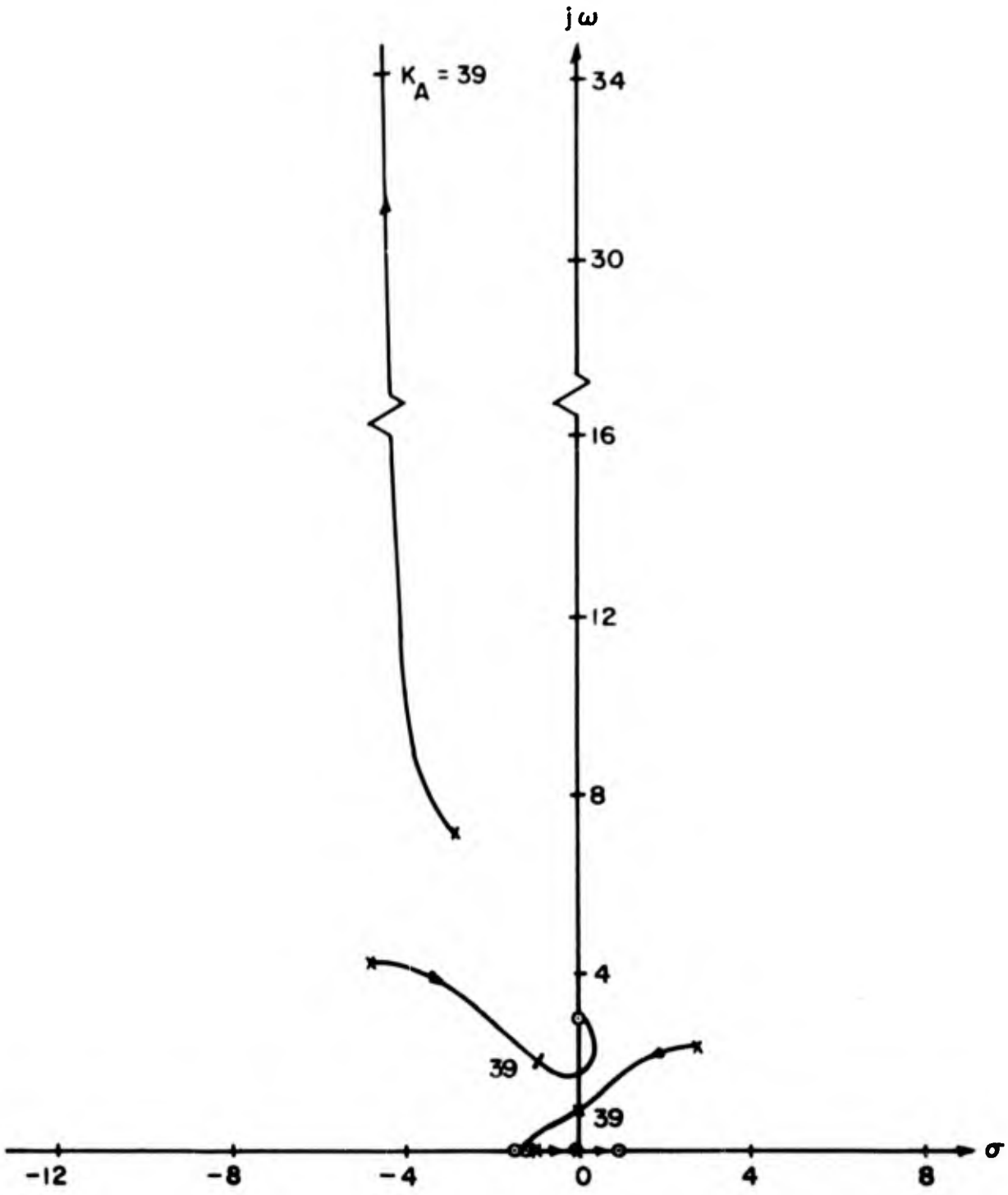

Figure 16. Root Locus of (θ_1/δ_1)
(K_c = 10; K_R = .625; K_z = .054; sensor at sta 140)

BLANK PAGE

SECTION VI

CLOSED-LOOP TRANSIENT DYNAMICS UNDER ACTIVE CONTROL - TWO INNER-LOOP SENSORS

Consider the system shown in Figure 17, where the inner loop now has two sensors providing linear rate and displacement feedback. Similar to the development of the previous section, the system of Figure 17 can be put in the equivalent form of Figure 18, where

$$\frac{K_c}{s+K_c}\left(\frac{\bar{z}_1}{\delta}\right) = \frac{-K_c K_{z_a}(s+1)\left[\phi_1(z_a)\,Aq_1\,Nq_1 + \phi_2(z_a)\,Aq_2\,Nq_2\right]}{(s+K_c)\,\Delta} \tag{112}$$

$$\left(\frac{\bar{z}_2}{\bar{z}_1}\right) = \frac{K_{z_b}(s+1)\left[\phi_1(z_b)\,Aq_1\,Nq_1 + \phi_2(z_b)\,Aq_2\,Nq_2\right]}{K_{z_a}(s+1)\left[\phi_1(z_a)\,Aq_1\,Nq_1 + \phi_2(z_a)\,Aq_2\,Nq_2\right]} \tag{113}$$

$$K_A\left(\frac{\bar{\theta}_i}{\bar{z}_2}\right) = \frac{K_A K_R A_\theta \left(s+\frac{1}{K_R}\right) N_\theta}{-K_{z_b}(s+1)\left[\phi_1(z_b)\,Aq_1\,Nq_1 + \phi_2(z_b)\,Aq_2\,Nq_2\right]} \tag{114}$$

To proceed further, one must specify sensor locations. For the time being arbitrarily select stations 300 and 140 for the z_a and z_b sensor, respectively. More will be said later concerning the effects of sensor location. For these locations, Equations 112, 113, and 114 have the numerical forms given below.

$$\frac{K_c}{s+K_c}\left(\frac{\bar{z}_1}{\delta}\right) = \frac{-48.8\,K_c K_{z_a}(s+1)(s-3.15\pm j\,2.65)(s+3.29\pm j\,3.84)\,s}{(s+K_c)(s-1.31)(s+1.543)(s+.012\pm j1.15)(s+.031\pm j\,3.051)s} \tag{115}$$

$$\left(\frac{\bar{z}_2}{\bar{z}_1}\right) = \frac{-135.6\,K_{z_b}(s+1)(s-3.2\pm j\,2.625)(s+3.315\pm j3.81)\,s}{48.8\,K_{z_a}(s+1)(s-3.15\pm j\,2.65)(s+3.29\pm j\,3.84)s} \tag{116}$$

$$K_A\left(\frac{\bar{\theta}_i}{\bar{z}_2}\right) = \frac{1.04\,K_A K_R\left(s+\frac{1}{K_R}\right)(s-1.148)(s+.00011)(s+1.343)(s+.027\pm j\,2.865)}{135.6\,K_{z_b}(s+1)(s-3.2\pm j\,2.625)(s+3.315\pm j\,3.81)s}. \tag{117}$$

The root locus for Equation 115 is shown in Figure 19. Notice it is nearly identical with the locus of Figure 15; however, the gain K_{z_a}, is negative for this sensor location. Using closed-loop roots corresponding to $K_{z_a} = -.144$, the open-loop transfer function for the second closure is

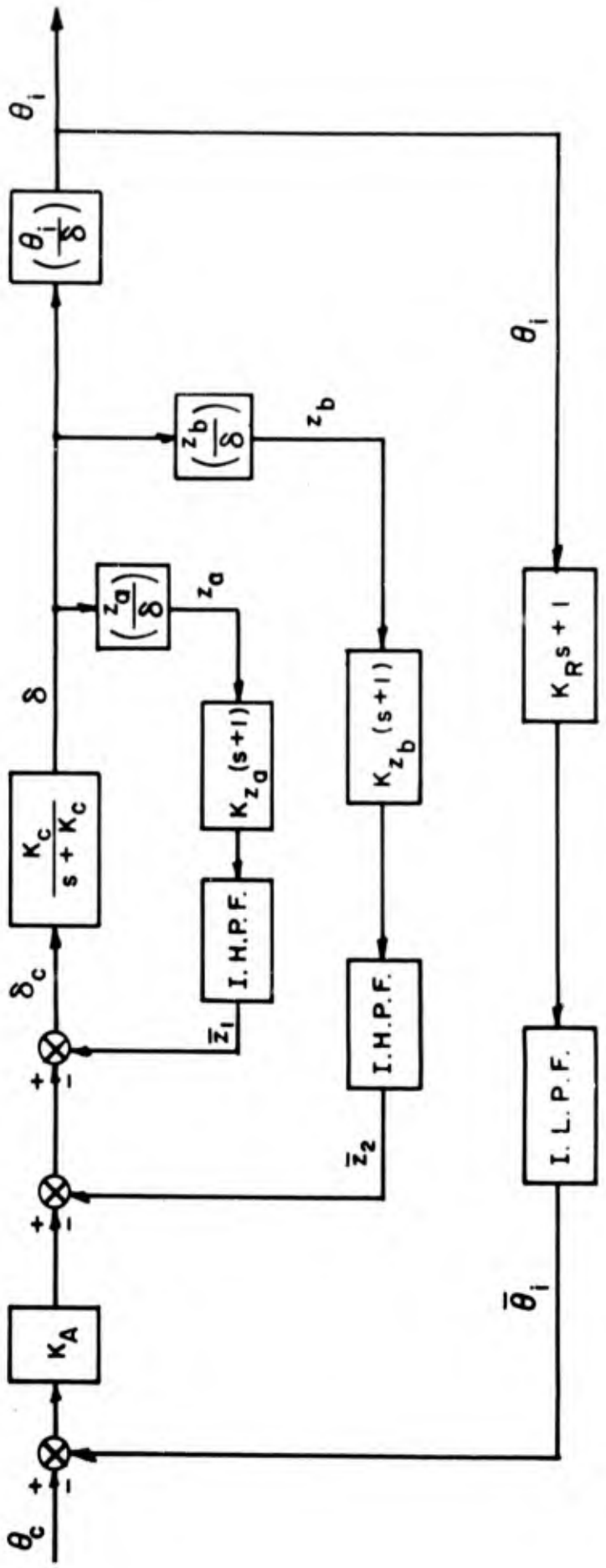

Figure 17. System Block Diagram

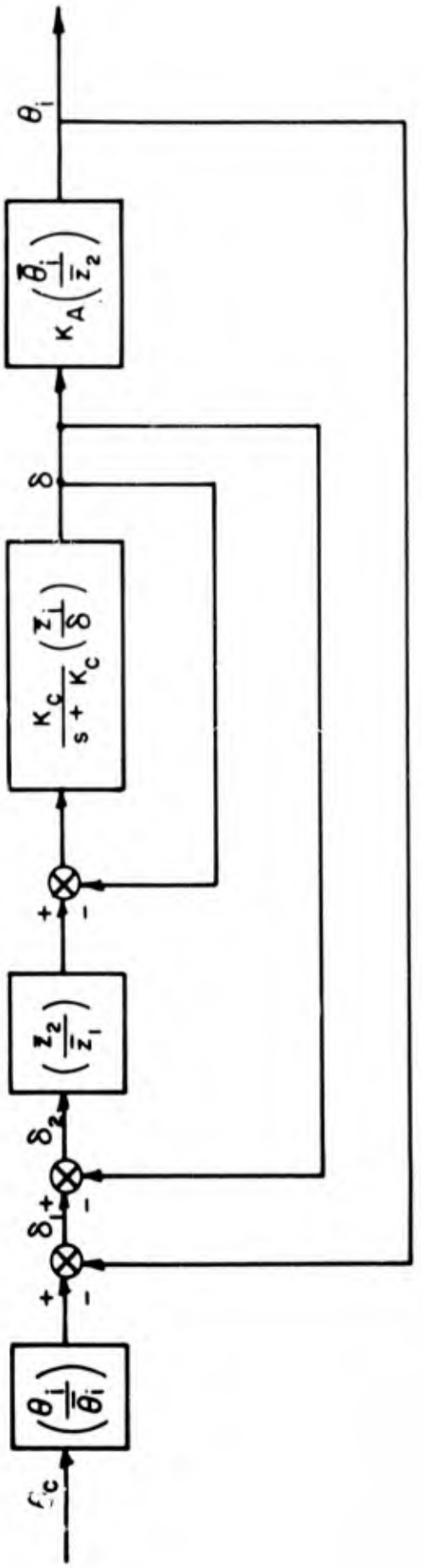

Figure 18. Equivalent System

$$\left(\frac{\delta}{\delta_2}\right) = \frac{1356 K_{z_b}(s+1)(s-3.2 \pm j\,2.625)(s+3.315 \pm j\,3.81)\,s}{(s+.9)(s-2.8 \pm j\,2.25)(s+2.55 \pm j\,6.8)(s+5 \pm j\,4.3)\,s} \cdot \qquad (118)$$

The root locus of Equation 118 is given in Figure 20. It is seen that the only significant effect produced by the second closure is to increase the second elastic mode frequency with increasing K_{z_b}. But this could be done with only the first loop closure by increasing K_{z_a}, as is evident in Figure 19. The second inner-loop sensor has provided no improvement in inner-loop characteristics as had been hoped for. Therefore the total closed-loop system will be no better than the simpler system of Figure 16.

Returning to the single inner-loop sensor case for a moment, observe in Figure 15 that the frequencies of both elastic modes could be increased if the zero in the right-half plane could be moved a considerable distance vertically. This zero is dependent on sensor location and is one of the roots of the equation

$$\phi_1(z)A_{q_1}N_{q_1} + \phi_2(z)A_{q_2}N_{q_2} = 0 \qquad (119)$$

where $\phi_1(z)A_{q_1}$ and $\phi_2(z)A_{q_2}$ are coefficients whose values depend on sensor location, and N_{q_1} and N_{q_2} are both normalized fifth-order polynomials in s. Numerous root locus analyses were made with the inner-loop sensor at various locations, but no location was found that would result in stiffening for both elastic modes simultaneously. Even if a location had been found that would do this, when the outer-loop is closed there would always be a branch of the locus corresponding to an elastic mode which would terminate on a zero lying on or relatively near the real axis. This zero is one of those in Equation 109, which are unalterable (short of configuration modification) except for the $(s + 1/K_R)$ factor, since they are due to the (θ/δ) transfer function. Even though the $(s + 1/K_R)$ factor is alterable, it still must lie on the real axis and will not change the situation.

Analysis has shown that the comments made above for the single-sensor case are equally true for the two-sensor results. It has thus been demonstrated that single or double sensor control of the inner-loop cannot simultaneously stiffen (increase frequency) both elastic modes with the outer-loop closed, using only single actuation. A possible recourse is to consider multiple actuation. That is, provide separate actuating systems for the two tasks of artificial structural stiffening and control of rigid-body motion. This will be investigated in Section VII.

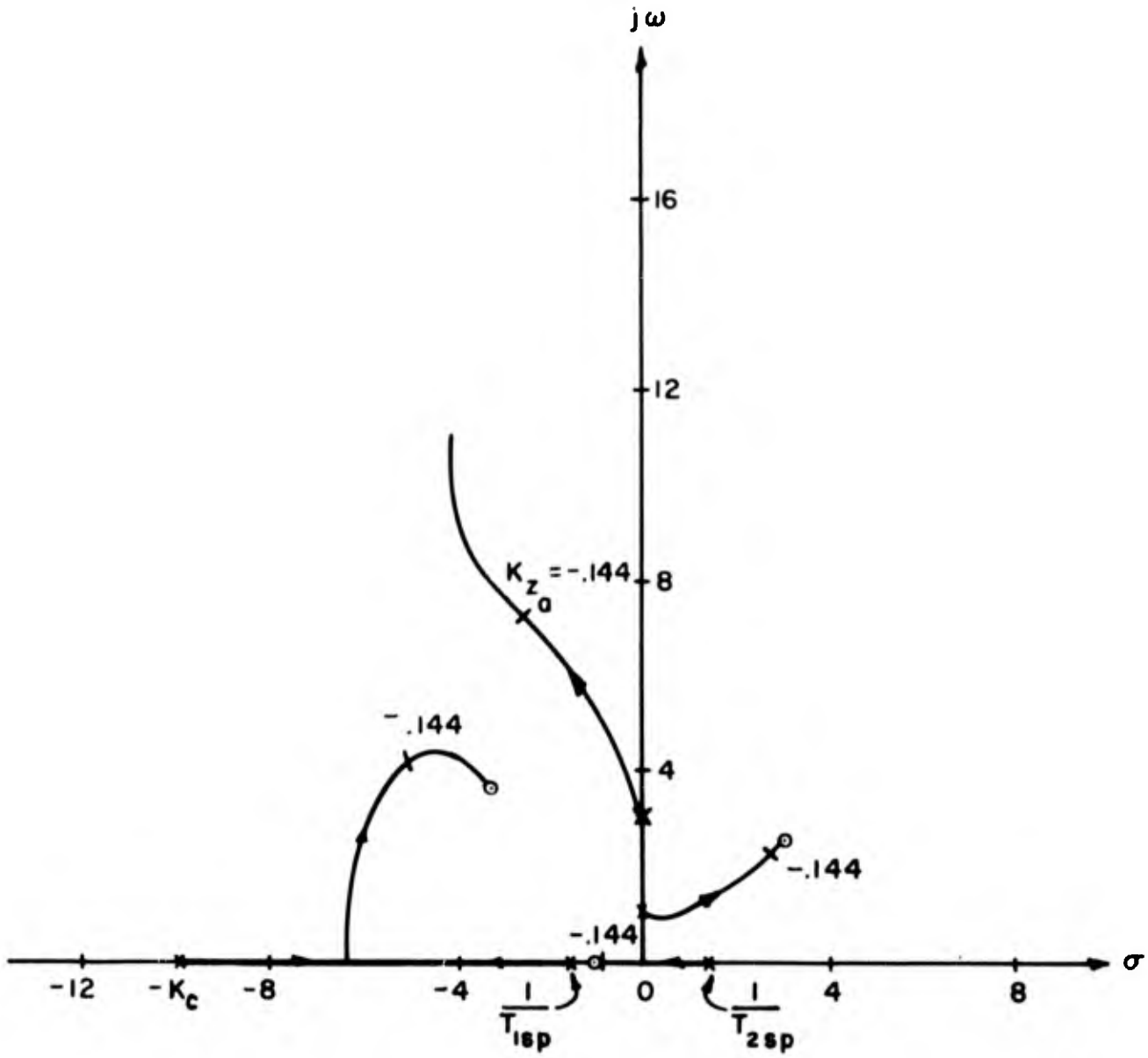

Figure 19. Root Locus of $\frac{K_c}{s+K_c}\left(\frac{\overline{Z}_1}{\delta}\right)$
(K_c = 10; sensor at sta 300)

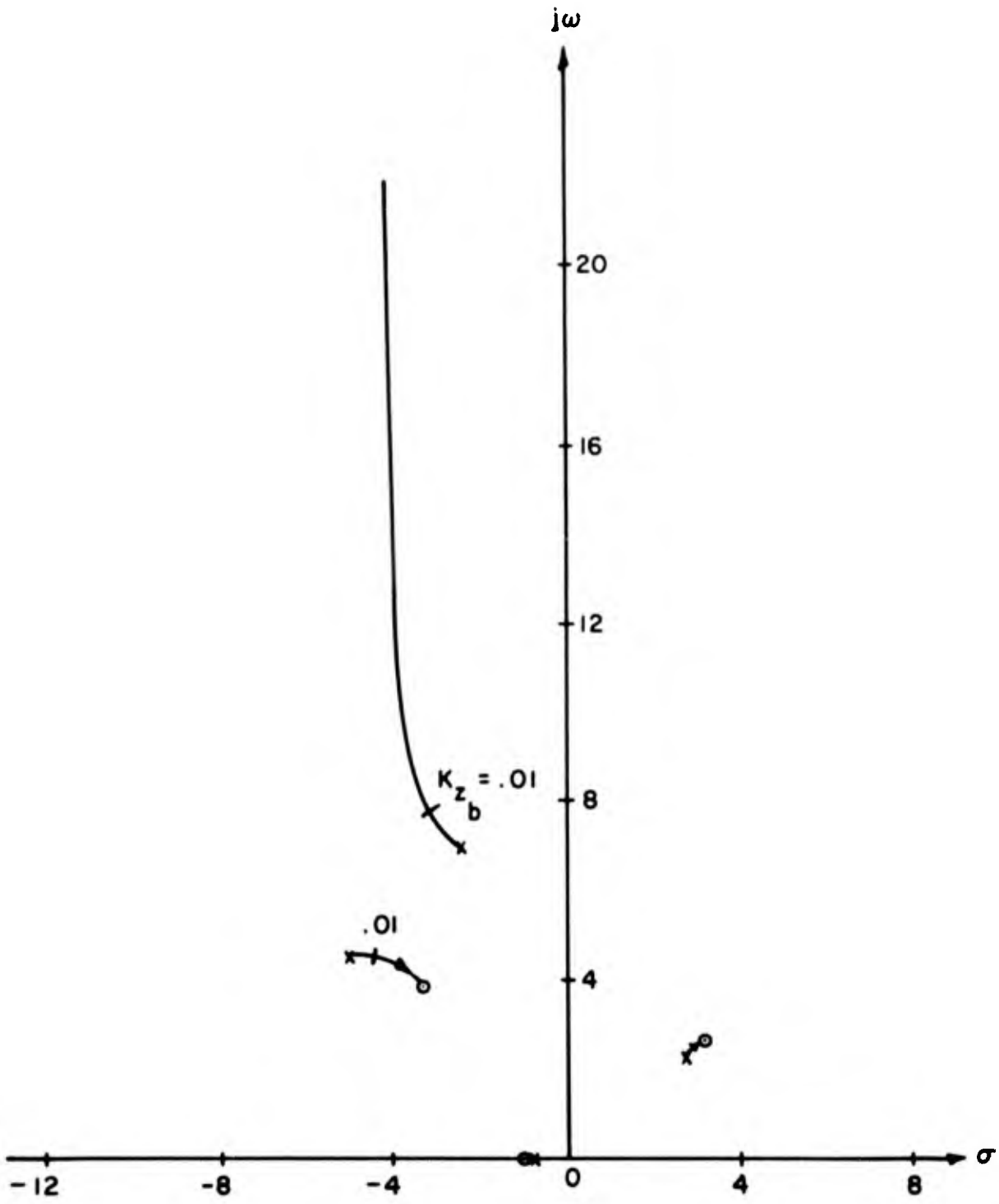

Figure 20. Root Locus of $\left(\frac{\delta}{\delta_z}\right)$
(K_c = 10; K_{z_a} = -.144; sensors at sta 300 and 140)

SECTION VII

DUAL ACTUATION
THRUST VECTORING PLUS SINGLE REACTION JET

By providing a suitably located and phased control force normal to the missile centerline and independent of the main engine thrust vector, it would seem possible to reduce the elastic displacements — resulting in an apparent stiffening of the structure with a corresponding increase in modal frequencies. Consideration will be given to the use of a single, dual-acting reaction jet for providing this force.

Assume the force F_r to be linearly proportional to the actuating signal δ_r of the valving mechanism and positive in the z - direction.

$$F_r = k\delta_r \tag{120}$$

where k is the proportionality constant. F_r will produce additional terms in the equations of motion derived in Section I. In particular, Equations 14, 15, 16, and 17 become

$$F_T = -T\left[\sigma_1(G)q_1 + \sigma_2(G)q_2 - \delta\right] + k\delta_r \tag{121}$$

$$M_T = -T\left\{\left[\ell_G\,\sigma_1(G) + \phi_1(G)\right]q_1 + \left[\ell_G\sigma_2(G) + \phi_2(G)\right]q_2 - \ell_G\delta\right\} + (\ell_r - \ell_{CG})\,k\delta_r \tag{122}$$

$$Q_{1T} = -T\left[\sigma_1(G)\phi_1(G)q_1 + \sigma_2(G)\phi_1(G)q_2 - \phi_1(G)\delta\right] + \phi_1(r)\,k\delta_r \tag{123}$$

$$Q_{2T} = -T\left[\sigma_1(G)\phi_2(G)q_1 + \sigma_2(G)\phi_2(G)q_2 - \phi_2(G)\delta\right] + \phi_2(r)\,k\delta_r\ . \tag{124}$$

When the terms containing δ_r are incorporated into Equation 29, one has

$$\begin{bmatrix} \text{Same as} \\ \text{in} \\ \text{Eq. 29} \end{bmatrix} \begin{Bmatrix} \alpha \\ \theta \\ q_1 \\ q_2 \end{Bmatrix} = \begin{Bmatrix} -Z_\delta \\ -M_\delta \\ -F_{1\delta} \\ -F_{2\delta} \end{Bmatrix} \delta + \begin{Bmatrix} -Z_{\delta_r} \\ -M_{\delta_r} \\ -F_{1\delta_r} \\ -F_{2\delta_r} \end{Bmatrix} \delta_r + \begin{Bmatrix} -Z_\alpha \\ -M_\alpha \\ -F_{1\alpha} \\ -F_{2\alpha} \end{Bmatrix} \alpha_g \tag{125}$$

where $Z_{\delta_r} = -\frac{k}{M} = -6.61 \times 10^{-6} k$

$$M_{\delta_r} = \frac{-k(\ell_r - \ell_{CG})}{I_y} = -6.545 \times 10^{-10} k (\ell_r - \ell_{CG})$$

$$F_{1\delta_r} = \frac{k\phi_1(r)}{m_1} = 1.61 \times 10^{-6} k\phi_1(r)$$

$$F_{2\delta_r} = \frac{k\phi_2(r)}{m_2} = 1.57 \times 10^{-6} k\phi_2(r) .$$

Assuming linear rate and displacement sensing of the elastic motion and first-order lag representation of the valve dynamics of the reaction jet, the closed-loop system takes the form shown in Figure 21. The high and low pass filters serve the same function as in the previous sections. At this point, a recently developed multiloop analysis and synthesis technique (Reference 4) will be introduced. The system of Figure 21 can be put in the form shown in Figure 22,

where

$$G_{12} = \frac{-K_z K_r \phi_1(z)(s+b)}{s + K_r} \tag{126}$$

$$G_{14} = \frac{-K_z K_r \phi_2(z)(s+b)}{s + K_r} \tag{127}$$

$$G_{21} = \frac{K_A K_c K_R \left(s + \frac{1}{K_R}\right)}{s + K_c} \tag{128}$$

and b in Equations 126 and 127 is a constant to be determined in the synthesis.

Omitting the details put forth in Reference 4, the (θ/θ_c) transfer function for the system of Figure 22 can be developed into the following form:

$$\left(\frac{\theta}{\theta_c}\right) = \frac{\left(\frac{A}{B}\right)}{\left[1 + \left(\frac{A}{B}\right)\right] K_R \left(s + \frac{1}{K_R}\right)} \tag{129}$$

where

$$\left(\frac{A}{B}\right) = G_{21}\left(\frac{\theta}{\delta}\right) \left[1 + \frac{-G_{12}\left(\frac{\theta}{\delta_r}\right) \frac{A_{q_1} N_{q_1}}{A_\theta N_\theta} - G_{14}\left(\frac{\theta}{\delta_r}\right) \frac{A_{q_2} N_{q_2}}{A_\theta N_\theta}}{1 + G_{12}\left(\frac{q_1}{\delta_r}\right) + G_{14}\left(\frac{q_2}{\delta_r}\right)} \right] . \tag{130}$$

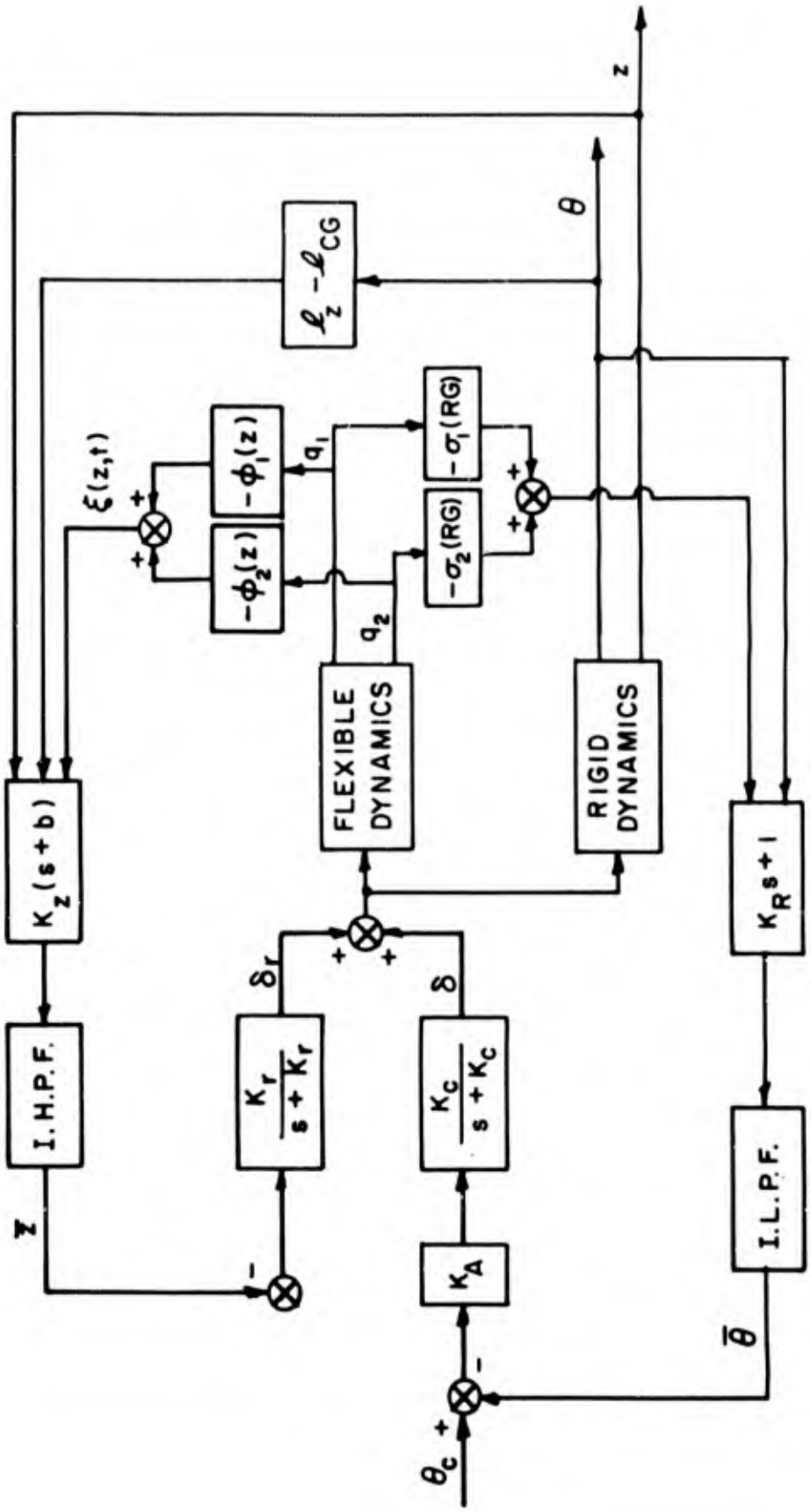

Figure 21. Diagram of Control by Dual Actuation (thrust vectoring plus single reaction jet)

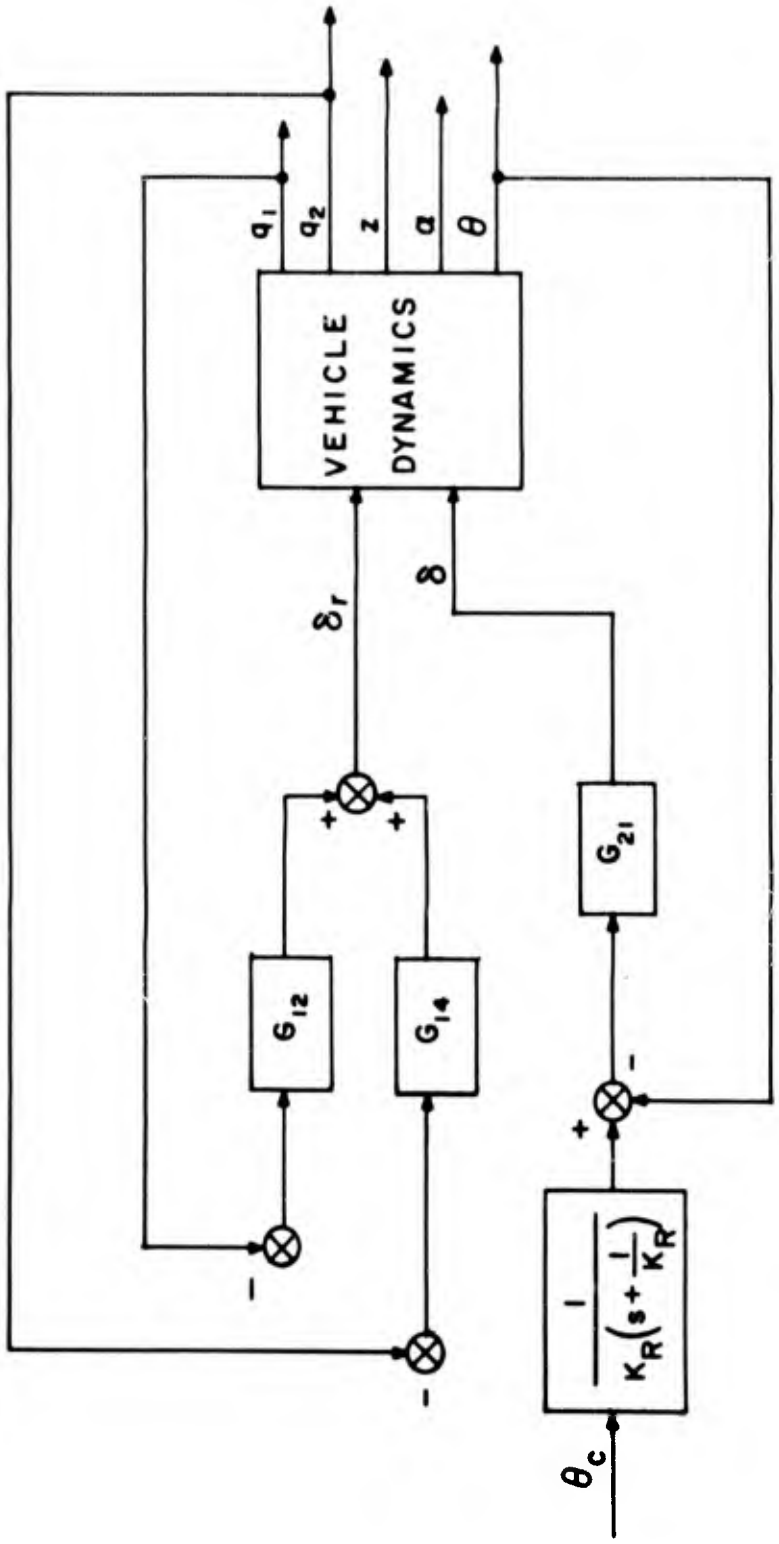

Figure 22. Unity Feedback Equivalent Diagram

Equations 129 and 130 are in a form suitable for root locus analysis involving three successive loop closures. These closures are shown in Figure 23. The open-loop transfer function of closure 1 contains the (q_1/δ_r) and (q_2/δ_r) transfer functions. These are obtained by applying Cramer's rule to Equation 125.

$$\left(\frac{q_1}{\delta_r}\right) = \frac{\begin{vmatrix} (1860s+51.6) & -1859s & 6.61\times10^{-6}k & (.01933s-7.66) \\ .1143 & (s^2+.0755s) & 6.55\times10^{-10}k(\ell_r-\ell_{CG}) & (-.000815s-.0097) \\ -29.3 & 3.27s & -1.61\times10^{-6}k\phi_1(r) & (-.0482s+5.107) \\ 8.55 & -1.96s & -1.57\times10^{-6}k\phi_2(r) & (s^2+.087s+8.181) \end{vmatrix}}{1860\,\Delta} \qquad (131)$$

$$\left(\frac{q_2}{\delta_r}\right) = \frac{\begin{vmatrix} (1860s+51.6) & -1859s & (-.0647s-4.682) & 6.61\times10^{-6}k \\ .1143 & (s^2+.0755s) & (.001326s-.087) & 6.55\times10^{-10}k(\ell_r-\ell_{CG}) \\ -29.3 & 3.27s & (s^2+.1285s+.312) & -1.61\times10^{-6}k\phi_1(r) \\ 8.55 & -1.96s & (-.05175s+2.013) & -1.57\times10^{-6}k\phi_2(r) \end{vmatrix}}{1860\,\Delta} \cdot \qquad (132)$$

By expanding the determinants in Equations 131 and 132, substituting into the open-loop transfer function of closure 1, and collecting terms, one has

$$\frac{\begin{aligned} &-.538\times10^{-6}kK_zK_r(s+b)\Big\{-\Big[3\phi_1(r)\phi_1(z)+2.92\phi_2(r)\phi_2(z)\Big]s^4+\Big[\phi_1(z)\Big(.194 \\ &-.003(\ell_r-\ell_{CG})-.488\phi_1(r)-.141\phi_2(r)\Big)+\phi_2(z)\Big(-.0565+.00239(\ell_r-\ell_{CG}) \\ &-.155\phi_1(r)-.678\phi_2(r)\Big)\Big]s^3+\Big[\phi_1(z)\Big(.0312+.0353(\ell_r-\ell_{CG})-24.85\phi_1(r) \\ &+14.9\phi_2(r)\Big)+\phi_2(z)\Big(-.003-.0102(\ell_r-\ell_{CG})+6.03\phi_1(r)-1.275\phi_2(r)\Big)\Big]s^2 \\ &+\Big[\phi_1(z)\Big(1.873-.0422(\ell_r-\ell_{CG})-1.95\phi_1(r)+1.19\phi_2(r)\Big)+\phi_2(z)\Big(-.408 \\ &+.00926(\ell_r-\ell_{CG})+.124\phi_1(r)-.865\phi_2(r)\Big)\Big]s+\Big[\phi_1(z)\Big(.1673+.344(\ell_r-\ell_{CG}) \\ &-3.07\phi_1(r)+.877\phi_2(r)\Big)+\phi_2(z)\Big(-.0192-.0748(\ell_r-\ell_{CG})+2.92\phi_1(r)+7.33\phi_2(r)\Big)\Big]\Big\}s \end{aligned}}{(s+K_r)\Delta} = -1 \qquad (133)$$

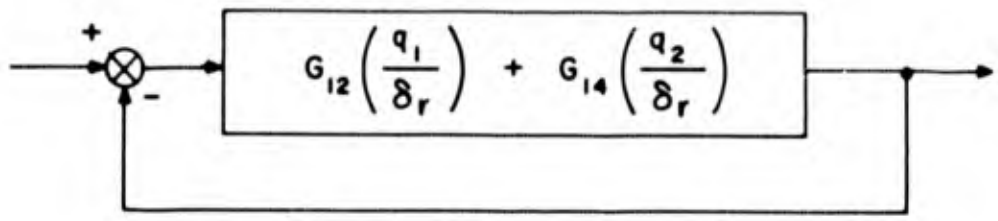

CLOSURE 1

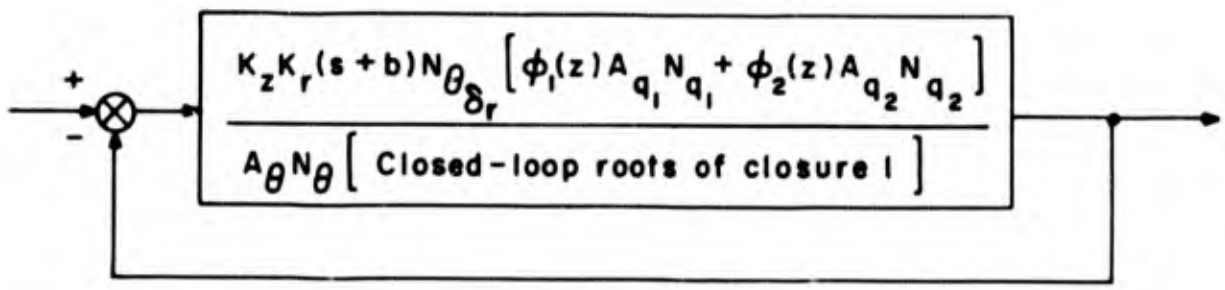

CLOSURE 2

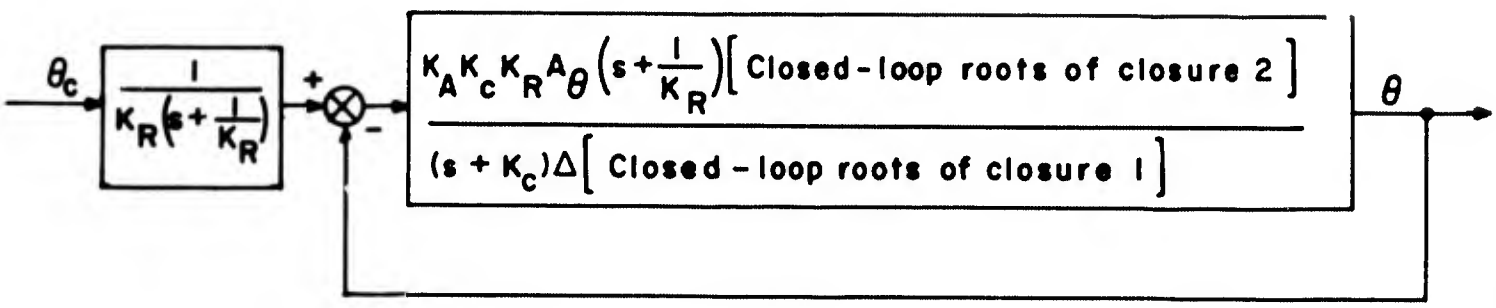

CLOSURE 3

Figure 23. Build-Up $\left(\frac{\theta}{\theta_c}\right)$ by Successive Loop Closures

It is evident that the zeros of Equation 133 are complicated functions of sensor and actuator locations. In order to perform closure 1 through root locus analyses of Equation 133, it is necessary to have numerical values for the open-loop poles and zeros. This requires that specific locations be chosen for the linear sensor and reaction jet actuator.

Twenty-four different combinations of sensor and actuator locations (tabulated in Table 3) were analyzed. The only combination which provided stiffening for both elastic modes was the sensor at station 39 and the reaction jet at station 140. For this combination, a root locus of Equation 133 is shown in Figure 24. K_r and b are taken as 10 and 3, respectively. One sees that the elastic mode frequencies can be increased at least a factor of 10 for sufficiently high gain. In this first closure the fact that the second mode is unstable along with a positive real root is not necessarily unacceptable since there are two more loops to be closed before the final closed-loop dynamics are determined. Also, as would be expected, this closure produced very little effect on the real roots corresponding to short-period motion.

TABLE 3

SENSOR-ACTUATOR COMBINATIONS

CASE	SENSOR STATION	ACTUATOR STATION
1	56	56
2	140	56
3	188	56
4	236	56
5	56	140
6	140	140
7	188	140
8	236	140
9	56	188
10	140	188
11	188	188
12	236	188

CASE	SENSOR STATION	ACTUATOR STATION
13	56	236
14	140	236
15	188	236
16	236	236
17	56	395
18	140	395
19	188	395
20	236	395
21	186	56
22	39	140
23	231	140
24	55	188

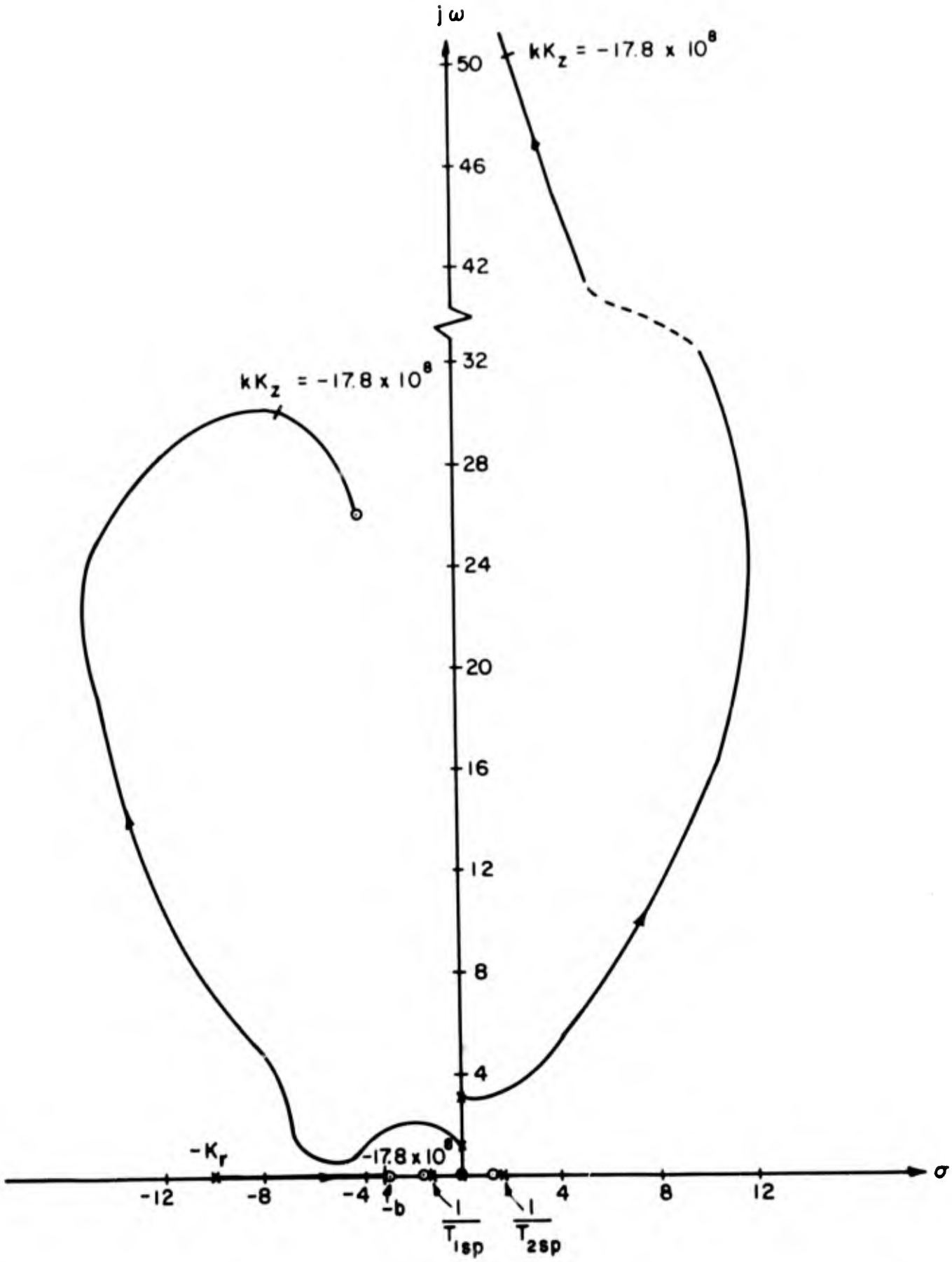

Figure 24. Root Locus of Equation 133, Closure 1
(K_r = 10; b = 3; sensor at sta 39; jet at sta 140)

Closure 2 is made on the following open-loop transfer function contained in Equation 130:

$$\frac{-G_{12}\left(\frac{\theta}{\delta_r}\right)\frac{A_{q_1}N_{q_1}}{A_\theta N_\theta} - G_{14}\left(\frac{\theta}{\delta_r}\right)\frac{A_{q_2}N_{q_2}}{A_\theta N_\theta}}{1 + G_{12}\left(\frac{q_1}{\delta_r}\right) + G_{14}\left(\frac{q_2}{\delta_r}\right)} .$$

Incorporating the expression for G_{12} and G_{14} and the closed-loop roots of closure 1, the equation for closure 2 becomes

$$\frac{K_z K_r (s+b) N_{\theta_{\delta_r}} \left[\phi_1(z) A_{q_1} N_{q_1} + \phi_2(z) A_{q_2} N_{q_2} \right]}{A_\theta N_\theta \left[\text{Closed-loop roots of closure 1} \right]} = -1 \qquad (134)$$

where $N_{\theta_{\delta_r}}$ is the numerator polynomial of (θ/δ_r) and is obtained by another application of Cramer's rule to Equation 125.

$$N_{\theta_{\delta_r}} = 6.61 \times 10^{-6} k (s-1.348)(s-28.121)(s+1.513)(s+.3 \pm j\,3.648)s . \qquad (135)$$

As indicated on Figure 24, for a gain of $kK_z = -17.8 \times 10^8$, the closed-loop roots of closure 1 are:

$$(s+3.01)(s-1.229)(s+1.645)(s+6.7 \pm j\,29.8)(s-2.7 \pm j\,50)s .$$

This gives the following numerical form for Equation 134:

$$\frac{\begin{array}{l}1.115 \times 10^7 (s+3)(s-1.348)(s-28.121)(s+1.513)(s+.3 \pm j\,3.648) \\ \quad \times (s+.00817 \pm j\,2.504)(s-1.612)(s+2.005)s^2\end{array}}{\begin{array}{l}(s-1.148)(s+.00011)(s+1.343)(s+.027 \pm j2.865)(s+6.7 \pm j\,29.8) \\ \quad \times (s-2.7 \pm j\,50)(s+3.01)(s-1.229)(s+1.645)s\end{array}} = -1 . \qquad (136)$$

The closed-loop roots of Equation 136 and thus closure 2 are

$$\begin{array}{l}(s+10^7)(s+2.995)(s+2.001)(s+1.515)(s-.001)(s-1.345)(s-1.616) \\ \quad \times (s-28.118)(s+.006 \pm j\,2.5)(s+.3 \pm j\,3.64)s\end{array}$$

From the open-loop transfer function expression for closure 3 given in Figure 23 and using the above numerical values, the equation for closure 3 is

$$\frac{1.04 K_A K_c K_R\left(s + \frac{1}{K_R}\right)(s+10^7)(s+2.995)(s+2.001)(s+1.515)\times (s-.001)(s-1.345)(s-1.616)(s-28.118)(s+.006\pm j2.5)(s+.3\pm j3.64)s}{(s+K_c)(s+1.543)(s-1.31)(s+.012\pm j1.15)(s+.031\pm j3.051)(s+6.7\pm j29.8)\times(s-2.7\pm j50)(s+3.01)(s+1.645)(s-1.229)s^2} = -1. \quad (137)$$

A few attempts at synthesizing an acceptable system through root locus analysis of Equation 137 quickly brought out the hopelessness of the task. A typical plot shown in Figure 25 will be used to illustrate the difficulties. All other attempts using various values for K_c and K_R led to the same difficulties discussed below.

Clearly, the system of Figure 25 is unstable due to four closed-loop roots in the right-half plane; and there is no apparent combination of values for K_c and K_R and compensating poles and zeros which could be introduced to stabilize the system. Also, all meaning associated with short-period and elastic mode components of the transient dynamics has been lost. There is no short-period mode which can be traced as emanating from the, not two, but now four open-loop short-period poles. There are now four pairs of complex open-loop poles corresponding to the two elastic modes — again, the identity of closed-loop first and second elastic modes is lost.

The design philosophy which was adopted in the beginning of this investigation and which has been touted by others interested in the general problem of mode interaction has proved invalid. Using auxiliary control inputs to increase the frequencies of the elastic modes sufficient to reduce the interaction in the forward-loop is a false notion. The fallacy in this philosophy is that the frequencies which are being increased are the closed-loop, coupled elastic mode frequencies and not the free-free bending mode undamped natural frequencies, which are unalterable, short of mass and stiffness modification of the basic-vehicle structure. And it is these free-free bending modes which are producing the mode interaction with the rigid-body motion. Thus, this is the reason the active control has failed to result in effectively decoupled elastic and rigid-body dynamics as had been intended.

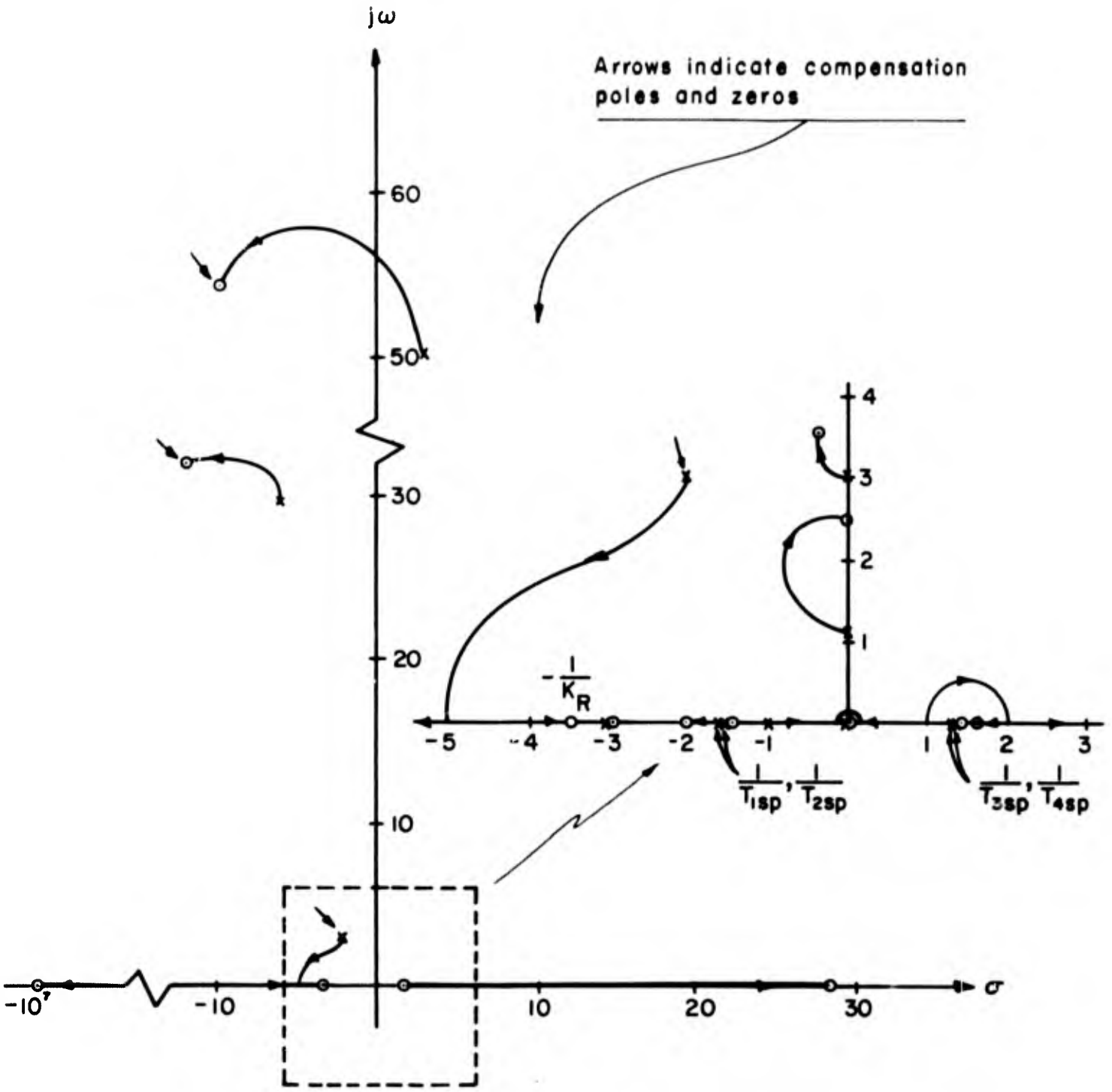

Figure 25. Root Locus of Equation 137, Closure 3
(K_r = 10; b = 3; $kK_z = -17.8 \times 10^8$; K_c = 1; K_R = .286;
sensor at sta 39; jet at sta 140)

BLANK PAGE

SECTION VIII

CONCLUSIONS AND RECOMMENDATIONS

CONCLUSIONS

1. The major conclusion drawn from this investigation is that the active control philosophy of using auxiliary control inputs to increase the frequencies of the elastic modes sufficient to reduce the mode interaction in the forward-loop is a false notion. It is the free-free bending modes which interact with the rigid-body motion, and input forces cannot alter their mode shapes and frequencies. They can be altered only by mass and structural stiffness changes to the basic vehicle. The input forces result in changes to elastic mode couples frequencies and damping ratios which do not affect the mode interaction phenomenon as defined in this report.

2. The mode interaction phenomenon is a direct result of aerodynamic coupling between free-free elastic modes and rigid-body degrees of freedom and can be reduced only by relocation of aerodynamic surfaces, reduction in aerodynamic surface area, increase in free-free elastic mode frequencies by mass and stiffness modifications of the structure, or combination of the three cures.

3. Preliminary control system design must include the significant elastic modes when mode interaction is present. A rigid-body-only synthesis will not yield "ball-park" values for the control element gains. The interaction can cause a rigid-body static divergence for an aerodynamically statically stable configuration in the uncontrolled or forward-loop-only case.

4. In applying multiloop analysis and synthesis techniques (such as those put forth in Reference 4) to vehicles susceptible to severe mode interaction, one discovers that many of the open-loop poles and zeros in the various loop closures are extremely close together. This presents the distinct possibility that slight changes in parameters can alter the relative locations of these poles and zeros and thus drastically affect the system closed-loop dynamics.

5. It is meaningless to specified desired transient response in terms of closed-loop short-period frequency and damping ratio as a criterion for control system synthesis when the vehicle is subject to severe mode interaction. In that case, the closed-loop modes cannot be identified as being elastic or rigid-body in the conventional sense, so new synthesis criteria are needed. Perhaps a better approach would be to specify desired time histories for the various output variables such as θ, α, q_1, and q_2.

6. Active control of elastic modes for the worthy purpose of load reduction can likely be achieved through control design if little mode interaction exists. The main advantage of such control would be to augment elastic mode damping, thereby reducing loads; it cannot be used for relieving mode interaction in the forward-loop.

7. It is important to start control system synthesis with a valid control philosophy. Servo techniques such as used herein can just as readily be applied to an invalid philosophy, but one will waste considerable effort trying to arrive at a workable system which is not attainable with the erroneous philosophy adopted at the start.

RECOMMENDATIONS

1. In future large booster designs the lifting surface area should be reduced to an absolute minimum to avoid severe mode interaction. Lifting surfaces should not be used to provide static stability, if avoidable; thrust vector control should be used.

2. One should take care to have a valid control philosophy before proceeding with detailed synthesis; although, as was the case in this study, synthesis attempts may be required to verify or reject the philosophy.

3. Work should be devoted to developing new transient dynamic response design criteria for vehicles exhibiting severe mode interaction. The concepts of closed-loop short-period and elastic modes of motion are mostly meaningless in this situation — particularly so when multiple control inputs are used. Criteria in terms of output time histories may be more appropriate.

4. When mode interaction exists, the effects of including the longitudinal equation of motion in the x-direction should be evaluated in order to verify the use of the two-degree-of-freedom short-period approximation to the rigid-body equations of motion.

5. Although the basic forward-loop coupling cannot be actively controlled, research is needed to arrive at a control philosophy which will eliminate mode interaction instabilities— the approach outlined in Reference 5 using optimal control theory appears promising and should be tried on the mode interaction problem.

SECTION IX

REFERENCES

1. Swaim, R. L. A General Theory and Analysis of the Dynamic Stability of Flexible-Bodied Missiles. ASD-TDR-62-627. Aeronautical Systems Division, Wright-Patterson Air Force Base, Ohio. October 1962.

2. Lukens, D. R., Schmitt, A. F., and Broucek, G. T. Approximate Transfer Functions for Flexible-Booster-and-Autopilot Analysis. WADD-TR-61-93. Wright Air Development Division, Wright-Patterson Air Force Base, Ohio. General Dynamics Corporation, San Diego, Calif. Contract No. AF 33(616)-7037. April 1961.

3. Bisplinghoff, R. L., Ashley, H., and Halfman, R. L. Aeroelasticity. Addison-Wesley, Cambridge, Mass. 1955.

4. McRuer, D. T., Ashkenas, I. L., and Pass, H. R. Analysis of Multiloop Vehicular Control Systems, ASD-TDR-62-1014. Aeronautical Systems Division, Wright-Patterson Air Force Base, Ohio. Systems Technology, Inc., Inglewood, Calif. Contract No. AF 33(616)-8024. March 1964.

5. Rynaski, E. G., Reynolds, P. A., and Shed, W. H. Design of Linear Flight Control Systems Using Optimal Control Theory, ASD-TDR-63-376. Aeronautical Systems Division, Wright-Patterson Air Force Base, Ohio. Cornell Aeronautical Laboratories, Inc., Buffalo, New York. Contract No. AF 33(657)-7498. April 1964.